UCL Université catholique de Louvain

École polytechnique de Louvain (EPL)

# Numerical study of tides in the subsurface oceans of icy satellites, with a particular focus on Saturn's moon Titan

Dissertation presented by
**Ange Pacifique ISHIMWE**

for obtaining the Master's degree in
**Mathematical Engineering**

Supervisor(s)
**Eric DELEERSNIJDER**

Reader(s)
**Véronique DEHANT, Julien HENDRICK , David VINCENT**

Academic year 2017-2018

*"Choose a job you love, and you will never have to work a day in your life. "*

Confucius

# *Abstract*

Rocky moons like the Moon are the most famous moons in general culture. However, there exist others types such as the icy moons. As their name suggests, they are celestial bodies mainly composed of ice. Their crust and others internal layers are made of ice. Titan, Europa or Ganymede are a few examples. Nevertheless, recent research discovered that a global subsurface ocean stand below the crust of some. The existence of such oceans is quite surprising given the low prevailing temperature at their surface. One of the principal hypotheses for the heat source comes from the tides of these ocean. More precisely, the kinetic energy dissipation generated by the tidal motion should help maintaining the ocean liquid. Moreover, the dissipations could influence some orbital parameters. Therefore, studying these tides is important.

In this master's thesis, the interest is brought to Titan. A numerical study of the tidal motion will be done in function of the nature of the crust. Using the Second-generation Louvain-la-Neuve Ice-ocean Model created by professors of the Université Catholique de Louvain-la-Neuve, the elevation and others characteristics of the tidal flow are generated in function of the model for the icy crust. A parametric study is then made. The parameters depends on the model of the surface. This study will show how the characteristics of Titan can influence the tidal motion.

*Keywords : Titan, SLIM, Tides, Icy moon, Tidal potential, Love number*

# *Acknowledgements*

Many thanks to the professor Eric Deleersnijder for accepting to be my supervisor. A lot of thanks to David Vincent for his help and all his kindness when I had problems with SLIM. Thank you both for your time and your insightful advices.

I am grateful to professor Veronique Dehant and professor Julien Hendrick for agreeing to spend time to read my master's thesis and be part of my jury.

Many thanks to my wonderful and loving parents and sisters, for their support during my whole academic path.

# Contents

# List of Figures

# List of Tables

# List of Abbreviations

| | |
|---|---|
| **GSO** | **G**lobal **S**ubsurface **O**cean |
| **UCL** | **U**niversité **C**atholique de **L**ouvain-la-Neuve |
| **SLIM** | **S**econd-generation **L**ouvain-la-Neuve **I**ce-ocean **M**odel |
| **SWE** | **S**hallow-**W**ater **E**quations |

# List of Symbols

**State of art**

| | | |
|---|---|---|
| $\mathbf{u}$ | Velocity vector of the flow | $\mathrm{m\,s^{-1}}$ |
| $\mathbf{d}$ | Deformation vector of the structure | m |
| $\eta$ | Elevation | m |
| $d$ | Deformation of the structure in the z-direction | m |
| $\sigma_s$ | Cauchy stress tensor | $\mathrm{N/m^2}$ |
| $p$ | Pressure | Pa |
| $\mathbf{I}$ | Identity matrix | |
| $\mu$ | Viscosity | Pa s |
| $R$ | Mean radius of Titan | m |
| $h$ | Depth of the ocean | m |
| $\delta$ | Aspect ratio | |
| $\rho$ | Density | $\mathrm{kg\,m^{-1}}$ |
| $t$ | Time | s |
| $\mathbf{g}$ | Gravitational acceleration | $\mathrm{m/s^2}$ |
| $\nu_t$ | Turbulent viscosity | Pa s |
| $w$ | Velocity in the z-direction | $\mathrm{m\,s^{-1}}$ |
| $H$ | Height of the water column | m |
| $\bar{\mathbf{u}}$ | Depth-averaged horizontal velocity | $\mathrm{m\,s^{-1}}$ |
| $\tilde{\mathbf{u}}$ | Turbulent part of the velocity | $\mathrm{m\,s^{-1}}$ |
| $\tau_s$ | Surface stress vector | Pa |
| $\tau_b$ | Bottom stress vector | Pa |
| $p_s$ | Surface pressure | Pa |
| $\epsilon_s$ | Spatial relaxation factor | |
| $\epsilon_t$ | Temporal relaxation factor | |
| $h_2$ | Radial tidal Love number | |
| $U$ | Tidal potential | $\mathrm{m^2/s^2}$ |

**Results of the free case**

| | | |
|---|---|---|
| $T$ | Period of a day | s |
| $\omega$ | Angular frequency | rad |

**Results of the Tidal potential**

| | | |
|---|---|---|
| $h_{2r}$ | Real part of the radial tidal Love number | |
| $h_{2i}$ | Imaginary part of the radial tidal Love number | |
| $\bar{\rho}$ | Average density of the ocean | $\mathrm{kg\,m^{-1}}$ |
| $\delta\rho$ | Difference between the average density of the ocean and the density of the crust | $\mathrm{kg\,m^{-1}}$ |

*Dedicated to my dear parents who have always been my great inspirations and my engines in my life.*

# Chapter 1

# Introduction

"*Space: the final frontier. These are the voyages of the starship Enterprise. Its five-year mission: to explore strange new worlds. To seek out new life and new civilizations. To boldly go where no man has gone before!*" (James T. Kirk, 1966)

I took the liberty to start with this quotation by the Captain of the Starship Enterprise because the motivations between my master thesis and his voyages are the same. We both want to study the beautiful mysteries of Space. However, I do not need to travel across many celestial bodies or even across solar systems to do so; I just need to travel across one, Titan, which can be seen on figure 1.1.

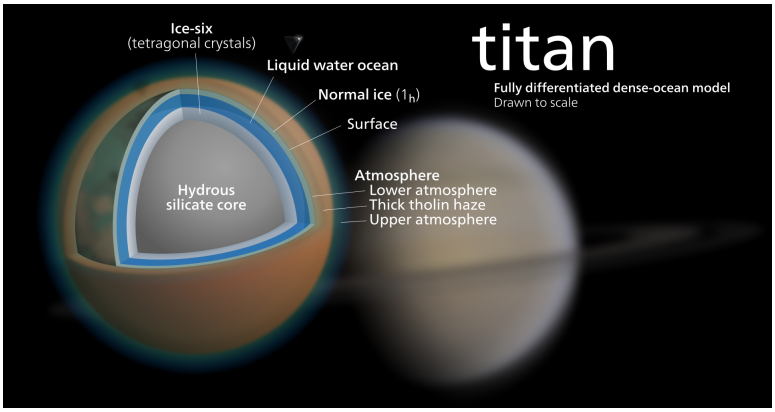


FIGURE 1.1: Representation of Titan
credit : [For11]/NASA

Titan is the biggest moon of Saturn and the $78^{th}$ one away from the Sun. It was discovered on March $25^{th}$, 1655 by the Dutch astronomer Christian Huygens. Inspired by Galileo's discovery of Jupiter's fourth largest moon, he decided to build a telescope with the help of his brother. By observing Saturn with one of his telescopes, he discovered a new moon behind its rings. It was Titan. NASA's Cassini Spacecraft and Huygens probe, which have been observing Saturn respectively from 2004 to 2017 and from 1997 to 2005, gathered information and measurements. Some of the information was incompatible with the hypothesis of Titan being completely solid. Its tilt and its moment of inertia did not make sense if the moon is a completely solid body. Furthermore, the information collected also showed curious rises of the surface. The actual rises seemed higher than the ones predicted. Therefore, the hypothesis of a global subsurface ocean (GSO) was considered. The main goal of my master's thesis is to numerically study the tides of this ocean and to find out how Titan's surface influence them.

Theses tides generate motion leading to kinetic energy dissipation in global oceans. This dissipation is the main source of heat along with the core of the moon. For this latter, thermal models tend to indicate that the core loses heat by convection[OF10]. Concerning the dissipation, the friction at the bottom and at the top of the ocean turns kinetic energy into heat. Therefore, it enables the ocean to stay liquid despite the low temperature at the surface. Furthermore, the dissipation could influence some orbital parameters because they rely on the energy dissipated within the moon. These two points constitute the main focus of the study of tides.

David Vincent, a teaching assistant from the Université Catholique de Louvain-la-Neuve (UCL) and a Collaborator of my master's thesis, has already modified a hydrodynamic model to be able to compute the tides of a global ocean underneath a certain surface. My objective is to study this behavior and compare it to the behavior of the tides taking into account the top of the ocean. I will use *SLIM*, the Second-generation Louvain-la-Neuve Ice-ocean Model. This program was created by professors of UCL. One of them was Eric Deleersnijder, one of my supervisors. This program allows to solve the shallow water equations by the means of finite elements. Now, get on board with me and let's start our journey beyond planet Earth.

# Chapter 2

# State of the art

## 2.1 Titan

Before describing my results, I'll shortly present two important aspects of this research : the current known specificities of Titan and the hydrodynamic model used to predict tides.

### 2.1.1 Global aspect

After Titan's discovery by Huygens, the first spatial mission that collected information was Voyager I in 1980. It was followed by Huygens probe and Cassini spacecraft as mentioned before. Together, they collected a lot of information on Titan's features. Titan, as said before, is one of Saturn's moons. More precisely, it is an icy moon. Titan is primarily composed of ice water and rocky material. It is the sixth gravitationally rounded moon from Saturn. This means that it is the sixth moon the closest from Saturn. Titan orbits at 10 Saturn radii. The radius of Titan is $2,575.0 \pm 2.0$ km and its mass is $(1.3452 \pm 0.0002)10^{23}$ kg. In other words, he is 50% larger than the Moon and 80% more massive. On figure 2.1, one can see that Titan is even larger than the Earth. Titan is the second largest moon of the Solar system after Ganymede, one of Jupiter's moons and it is more massive than Mercury, the smallest planet. A day corresponds to 15 days and 22,8 hours on Earth. This is also the orbital period. Thus, like the Moon and many of the satellites of the giant planets, **its rotational period is identical to its orbital period**. Consequently, Titan is tidally locked in synchronous rotation with Saturn, and permanently shows the same face to the planet just like the Moon with the Earth. What's more, the gravity on Titan is equivalent to $0.14g$ or 0.80 the gravity of the Moon which means $1.352ms^{-2}$. In other words, on Titan, you would be able to jump 7 times higher than on Earth.

There are two kinds of tides acting on moons : the static and the dynamic tides. The former ones imply deformations that do not depend on time. There is no tidal motion. Titan being tidally locked in synchronous rotation with Saturn, it should only experiment static tides. Nevertheless, dynamic tides appear on Titan. They are generated by two specificities of its orbit : **the eccentricity of the orbit of Titan and its obliquity** . The two characteristics make Titan undergo a forcing entrained by Saturn's force of attraction. Actually, the Moon follows the same behavior. The tides generated are caused by the eccentricity of the orbit of the Moon and its obliquity.

### 2.1.2 Titan's surface and atmosphere

Titan's surface temperature is about 94.15 °K. This low temperature is due to the fact that Titan receives 1% of the sunlight the Earth receives. Then, 90% of this sunlight is

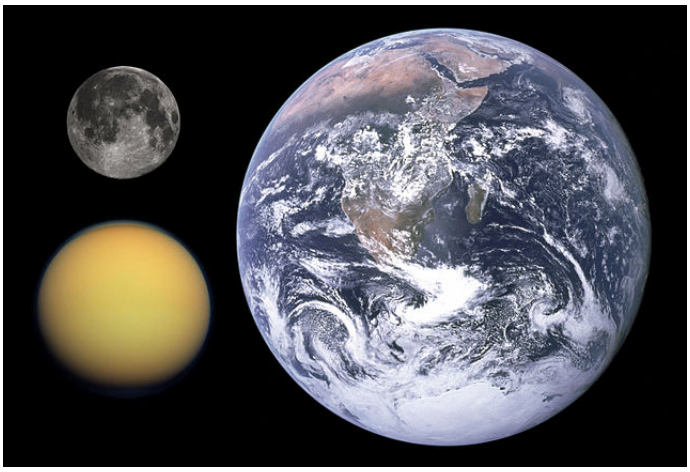

FIGURE 2.1: Comparison of Titan with the Earth and the Moon
credit : NASA/Gregory H. Revera

absorbed by the thick atmosphere of Titan. Thus, the surface of Titan only receives 0.01% less sunlight than the Earth. However, the methane in the atmosphere causes a greenhouse effect. The surface of Titan is at a thermal equilibrium.

Titan's atmosphere is composed of nitrogen (95%) and methane (5%) with trace amounts of other gases [Eri18]. High in the atmosphere, methane and nitrogen molecules are split apart by the sun's ultraviolet light and high-energy particles accelerated by Saturn's magnetic field; the products of this splitting recombine to form a variety of organic molecules.

The possibility of hydrocarbon seas, lakes and rivers on Titan was first based on Voyager 1 and 2 data that showed Titan to have a thick atmosphere of approximately the correct temperature and composition to support them [Eri18]. Cassini mission confirmed the existence of liquid methane on Titan. These seas and these lakes are filled by the cryovolcanoes. They erupt methane and ethane into the atmosphere, which then rains down onto the surface, forming lakes. The large ones are known as maria (seas) and the small ones as lacus (lakes). This means that Titan is the only celestial body of the solar system other than the Earth on which a fluid cycle similar to the hydrological cycle on Earth has been observed.

### 2.1.3 Internal structure

On figure 2.2, there are several examples of internal structures. One can see that the internal structure of each moon is represented by a succession of layers. Each moon has its own structure, some more complex than others. Some have an icy layer and others don't. Some even have even subsurface ocean like Titan.

The internal structure of this latter would be divided, from the surface to the center, into an layer composed of ice of type Ih, an ammonia-rich water liquid layer, a double high-pressure ice layer (phases V and VI), and a rocky core[For11]. The first ice layer is supposed to have a shell thickness of 100 km, a density of 930.9 kg $m^{-1}$ and a mass ratio of 5.6%. It follows the global ocean with a depth between 0 and 200 km, a density of 1023.5 kg $m^{-1}$ and a mass ratio of 13.2. Then, a double ice layer lies with depths of 62 and 42 km, densities of 1272.7 and 1338.9 kg $m^{-1}$ and mass ration of 3.5 and 2.7 %. Finally, there is a silicate core made of iron and rock[Rus04] with a density of 2542.3 kg $m^{-1}$ and a mass ratio of 75%. Actually, the internal structure of

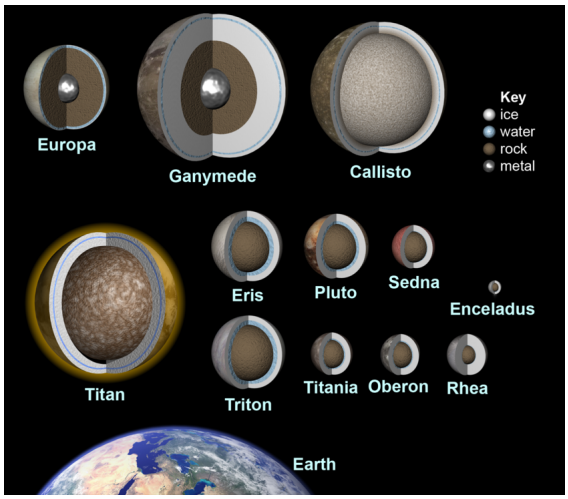


FIGURE 2.2: Different internal structures of icy bodies
credit : The Planetary Society

the Earth can be seen like Titan's. The subsurface ocean of Titan could be seen as the Earth's mantle.

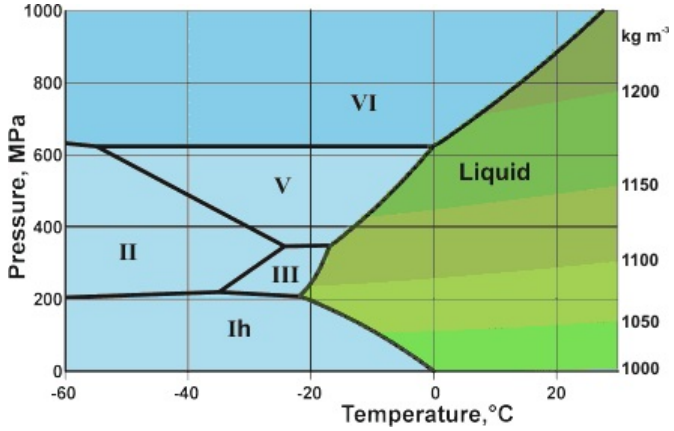


FIGURE 2.3: Different phases of ice.
**I** : Normal hexagonal crystalline ice. **II** : A rhombohedral crystalline form with highly ordered structure. **III** : A tetragonal crystalline ice. **V** : A monoclinic crystalline phase. **VI** : A tetragonal crystalline phase.
credit : Martin Chaplin

Previously, I described different types of ice. Depending on the pressure and temperature conditions, the ice layer will be made of one or another type of ice. This latter can obtain different crystalline structures. In the case of Titan, the interesting ones are the ice of type I,V and VI. The first corresponds to the normal and hexagonal crystalline ice. The second one corresponds to a monoclinic crystalline phase. It is the most complicated structure. The last one corresponds to a tetragonal crystalline phase. All the conditions to obtain ice are shown on figure 2.3 .

### 2.1.4 Similar moons

In the previous section, the figure 2.2 showed different internal structure. Let's look at them again to enumerate the major existing differences. Icy bodies can be made of only a rock core and an ice layer like Rhea. To this, one can add a core made of iron

as Europa. Of course, a global ocean can also occur. However, this global ocean can lie at different places. For instance, in the icy celestial bodies Pluto, Eris and Triton, it directly follows the silicate core. It can finally be between ice layers.

## 2.2 Physical model

### 2.2.1 Visco-elastic model

In the previous section, I discussed the origins of tides on Titan. One can study the tidal response of a global subsurface ocean by mean of a hydrodynamic model. Nevertheless, there is an icy crust at the top of the GSO which modifies its dynamic. Furthermore, the moons with an ocean are not the only ones to have tides. Fully solid moons also have them. In this context, a fluid-structure interaction (FSI) approach can be interesting.

Usually, the tidal responses in this approach are simulated by means of visco-elastic models (e.g. [FSL03][GTS05]). These models consider the GSO as a layer which can decouple the icy crust from the core of the moon. They study the moon as a global object. The membrane approach to tidal deformations of a body with a subsurface ocean is based on three assumptions[Beu15b].

- Spherical symmetry: the interior structure of the undeformed body is assumed to be spherically symmetric so that density and viscoelastic properties vary radially but not laterally.
- Static limit: the tides are of long period so that dynamical terms can be neglected in the viscoelastic problem.
- Membrane approximation: the shell is thin, the transverse normal stress is negligible, the membrane suffer from extension but no bending or twisting and the strains are independent of depth

Each layer receives information from the neighboring layers and gives them information back. Finally, the deformation of the moon is obtained. The FSI approach being very complex, before starting it, one has to study different possible cases.

For Titan, the shell can have different behaviors. A purely elastic shell and a visco-elastic shell are two of them. The former one adds friction and its main effect is that the crust follows perfectly the motion of the GSO. Moreover, the shell will follow the deformation of the ocean. The second case also adds friction but the shell will deform with a phase shift. Therefore, it will have an impact on the elevation of the ocean.

#### Coupling problem

When one talks about interaction between a fluid and a structure, the exchanges between them are very important. It is the exchange of momentum and energy that is studied here. The two equilibrium conditions that have to be imposed at the interface are the following :

- kinematic conditions : $\mathbf{u} = \dot{\mathbf{d}}$ and $\eta = d$
  with $\mathbf{u}$ the velocity of the flow, $\mathbf{d}$ the deformation of the structure, $\eta$ the elevation of the ocean and $d$ the deformation of the structure in one z-direction
- dynamic condition : $\sigma_s n_s = -\sigma_f n_f$
  with $\sigma_s$ the Cauchy stress tensor and $\sigma_f = -p\mathbf{I} + \mu(\nabla\mathbf{u} + \nabla\mathbf{u}^T)$

To apply this two conditions, the flows and structure equations have to be coupled. There are two methods to do it[FG09] :

- Monolithic or fully coupled method : both systems are solved simultaneously. Thus, they form a large system of equations
- Partitioned or segregated method : both equations are solved one after another using for one the information given by the other via the boundary conditions. There are two ways to do so, a loose one and a strong one. The first one consists of computing the fluid and the structure characteristic once per time step. The second one consists in computing them using a high number of subiterations.

In my master's thesis, the method uses is the Monolithic method. However, this method is a little bit adapted and changed. This is described in the next subsection.

### 2.2.2 Hydrodynamic model

The visco-elastic model does not take into account the internal dynamics of the liquid layer such as the Coriolis term. Consequently, in my master's thesis, I will focus on the hydrodynamic model. I will study the tides of the GSO without a layer above it using SLIM and with a layer above it using SLIM modified. Thus, the GSO has a feedback from the solid layer but not the other way around. The deformations of the solid layer is used to constrain the GSO while it does not have influence on the solid model.

To predict the flow of the GSO, the shallow-water equations (SWE) are used. An illustration of the shallow-water system is shown on figure 2.4. These equations are derived from the mass and the momentum conservation equations under some assumptions.

- The density is constant or the density variation is weak with respect to the mean density
- The aspect ration is small (depth is much smaller than the horizontal characteristic length)

Actually, the first assumption is not respected in the GSO. Indeed, hydrothermal plumes are likely to occur due to geothermal heating from the sea floor. Such plumes form narrow cylindrical chimneys which broad to cone-shaped eddies of 10-35 km in diameter [GL12]. However, we only pay interest in the tidal dynamics, the plume dynamics is beyond the scope of this master's thesis. For this reason, we do not take them into account and we assume a constant density over the ocean. The second assumption depends directly on the moon. Indeed, the aspect ratios rely on the radius of the moon, R, and the depth of the ocean, h. For Titan, we do no have problem because the depth of the ocean in the literature is estimated at [0,200] km[1]. This gives the following aspect ratio :

$$\delta = \frac{200000}{2\pi 2575000} = 0.01236$$

[1] https://www.esa.int/Our_Activities/Space_Science/Cassini-Huygens/Titan_s_tides_point_to_hidden_ocean

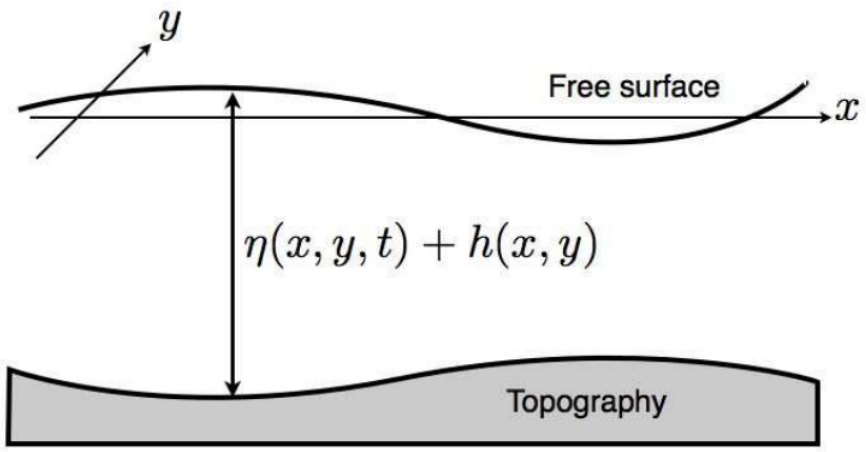


FIGURE 2.4: Schematic illustration of the shallow-water system

The assumptions checked, I will describe the development to obtain the SWE starting from the equations of conservation of mass and conservation of momentum (The Navier-Stoke equations) :

$$\frac{\partial \rho}{\partial t} + \boldsymbol{\nabla} \cdot (\rho \mathbf{u}) = 0$$
$$\frac{\partial (\rho \mathbf{u})}{\partial t} + \boldsymbol{\nabla} \cdot (\rho \mathbf{u}\mathbf{u}) + \rho \mathbf{g} = -\boldsymbol{\nabla} \mathbf{p} + \boldsymbol{\nabla} \sigma$$

Using the first assumption and the Stoke's stress constitutive equation, the equation can be simplified.

$$\boldsymbol{\nabla} \cdot \mathbf{u} = 0 \tag{2.1}$$
$$\frac{\partial \mathbf{u}}{\partial t} + \boldsymbol{\nabla} \cdot (\mathbf{u}\mathbf{u}) + \mathbf{g} = -\frac{1}{\rho} \boldsymbol{\nabla} \mathbf{p} + \boldsymbol{\nabla} \cdot (\nu_t [\boldsymbol{\nabla} \mathbf{u} + \boldsymbol{\nabla} \mathbf{u}^T]) \tag{2.2}$$

In the last big term, the divergence of the second term is null.

$$\begin{aligned} \boldsymbol{\nabla} \cdot (\boldsymbol{\nabla} \mathbf{u}^T) &= \boldsymbol{\nabla} (\boldsymbol{\nabla} \cdot \mathbf{u}) \\ &= 0 \end{aligned}$$

The equations become then simpler.

$$\boldsymbol{\nabla} \cdot \mathbf{u} = 0 \tag{2.3}$$
$$\frac{\partial \mathbf{u}}{\partial t} + \boldsymbol{\nabla} \cdot (\mathbf{u}\mathbf{u}) + \mathbf{g} = -\frac{1}{\rho} \boldsymbol{\nabla} \mathbf{p} + \boldsymbol{\nabla} \cdot (\nu \boldsymbol{\nabla} \mathbf{u}) \tag{2.4}$$

To these equations, we add two boundary conditions. The first condition imposes no normal flow at the seabed (impermeability condition). The second one imposes no relative normal flow at the air-sea interface.

$$\mathbf{u} \cdot \boldsymbol{\nabla} h + w = 0$$
$$\frac{\partial \eta}{\partial t} + \mathbf{u} \cdot \boldsymbol{\nabla} \eta - w = 0$$

The variables that will be used are

- The actual height of the water column

$$H(t,x,y) = \eta(t,x,y) + h(x,y)$$

- The depth-averaged horizontal velocity

$$\bar{\mathbf{u}}(t,x,y) = \frac{1}{H(t,x,y)} \int_{-h}^{\eta} \mathbf{u}(t,x,y,z)dz$$

Now, I integrate the (Boussinesq version of the) continuity equation from z = -h to z = $\eta$.

$$\begin{aligned} 0 &= \int_{-h}^{\eta} \boldsymbol{\nabla} \cdot \mathbf{u} dz \\ &= \int_{-h}^{\eta} \boldsymbol{\nabla} \cdot \mathbf{u} + \frac{\partial w}{\partial z} dz \\ &= \int_{-h}^{\eta} \boldsymbol{\nabla} \cdot \mathbf{u} dz + \int_{-h}^{\eta} \frac{\partial w}{\partial z} dz \end{aligned}$$

Since both $h$ and $\eta$ depend on t,x and y, I apply the Leibniz's integral rule.

$$\begin{aligned} 0 &= \int_{-h}^{\eta} \boldsymbol{\nabla} \cdot \mathbf{u} dz + \int_{-h}^{\eta} \frac{\partial w}{\partial z} dz \\ &= \boldsymbol{\nabla} \cdot \int_{-h}^{\eta} \mathbf{u} dz - \boldsymbol{\nabla}\eta \cdot [\mathbf{u}]_{z=\eta} + \boldsymbol{\nabla}(-h) \cdot [\mathbf{u}]_{z=-h} + [w]_{z=\eta} - [w]_{z=-h} \\ &= \boldsymbol{\nabla} \cdot (H\bar{\mathbf{u}}) + (-\boldsymbol{\nabla}\eta \cdot [\mathbf{u}]_{z=\eta} + [w]_{z=\eta}) - (\boldsymbol{\nabla}h \cdot [\mathbf{u}]_{z=-h} + [w]_{z=-h}) \end{aligned}$$

Using the boundary conditions , I obtain :

$$0 = \boldsymbol{\nabla} \cdot (H\bar{\mathbf{u}}) + \frac{\partial \eta}{\partial t} \tag{2.5}$$

This is the depth-integrated continuity equation.

Before I integrate over depth, the momentum equation for vertical velocity can be examined. By assuming that the wave length is much longer than the depth of the fluid (the second assumption), all of the terms except the pressure derivative and the gravity term are small. Then I deduce the hydrostatic pressure by integrating the vertical component of the momentum equation.

$$\begin{aligned} \int_{-h}^{\eta} \frac{\partial p}{\partial z} dz &= \int_{-h}^{\eta} -\rho g dz \\ p_s - p &= -\rho g(\eta - z) \end{aligned}$$

where $p_{os}$ is the pressure acting on the sea surface, $p(x,y,\eta,t) = p_s(x,y)$. This is the hydrostatic pressure distribution. Then,

$$\boldsymbol{\nabla} p = \rho g \boldsymbol{\nabla} \eta$$

Before going further, I have to introduce a new variable $\mathbf{u}'$, the turbulent part of the velocity $\mathbf{u}$. Thus,

$$\mathbf{u} = \bar{\mathbf{u}} + \mathbf{u}'$$

As the density variations are neglected, the average of the advection terms of the equations reads

$$\boldsymbol{\nabla} \cdot \overline{\mathbf{u}\mathbf{u}} = \boldsymbol{\nabla} \cdot (\bar{\mathbf{u}}\bar{\mathbf{u}}) + \boldsymbol{\nabla} \cdot \overline{\mathbf{u}'\mathbf{u}'}$$

Integrating the momentum equations over the water depth, I obtain the following results.

$$\begin{aligned}
\int_{-h}^{\eta} \frac{\partial \mathbf{u}}{\partial t} dz &= \frac{\partial H\bar{\mathbf{u}}}{\partial t} - \frac{\partial \eta}{\partial t}[\mathbf{u}]_{z=\eta} + \frac{\partial(-h)}{\partial t}[\mathbf{u}]_{z=-h} \\
&= \frac{\partial H\bar{\mathbf{u}}}{\partial t} - \frac{\partial \eta}{\partial t}[\mathbf{u}]_{z=\eta} \\
\int_{-h}^{\eta} \boldsymbol{\nabla} \cdot (\mathbf{u}\mathbf{u}) dz &= \boldsymbol{\nabla} \cdot [H\bar{\mathbf{u}}\bar{\mathbf{u}} + H\overline{\mathbf{u}'\mathbf{u}}] - [\mathbf{u}]_{z=\eta} \cdot \boldsymbol{\nabla}\eta[\mathbf{u}]_{z=\eta} + [{}'bfu]_{z=-h} \cdot \boldsymbol{\nabla}(-h)[\mathbf{u}]_{z=-h} \\
\int_{-h}^{\eta} \boldsymbol{\nabla} \cdot (\nu \boldsymbol{\nabla}\mathbf{u}) dz &= \int_{-h}^{\eta} (\nu \boldsymbol{\nabla}\mathbf{u}) \cdot n dz \\
&= \frac{\tau^s + \tau^b}{\rho}
\end{aligned}$$

The equation becomes :

$$\frac{\partial H\bar{\mathbf{u}}}{\partial t} + \boldsymbol{\nabla} \cdot [H\bar{\mathbf{u}}\bar{\mathbf{u}} + H\overline{\mathbf{u}'\mathbf{u}'}] + gH\boldsymbol{\nabla}\eta = \frac{\tau^s + \tau^b}{\rho}$$

I apply the Fourier-Fick parametrization.

$$\overline{\mathbf{u}'\mathbf{u}'} = -\nu_h[\boldsymbol{\nabla}\bar{\mathbf{u}} + (\boldsymbol{\nabla}\bar{\mathbf{u}})^T]$$

Considering the approximation that the second term is much smaller than the first, I obtain the equation.

$$\frac{\partial \bar{\mathbf{u}}}{\partial t} + \bar{\mathbf{u}} \cdot \boldsymbol{\nabla}\bar{\mathbf{u}} + g\boldsymbol{\nabla}\eta = \frac{1}{H}\boldsymbol{\nabla} \cdot (H\nu\boldsymbol{\nabla}\bar{\mathbf{u}}) + \frac{\tau^s - \tau^b}{\rho H} \tag{2.6}$$

Finally, adding the forcing of Saturn due to the gravity and the Coriolis term due to the rotation of the moon, I obtain the SWE of the hydrodynamic model.

$$\frac{\partial \bar{\mathbf{u}}}{\partial t} + \bar{\mathbf{u}} \cdot \boldsymbol{\nabla}\bar{\mathbf{u}} + f\mathbf{e}_z \wedge \bar{\mathbf{u}} + g\boldsymbol{\nabla}\eta = \frac{1}{H}\boldsymbol{\nabla} \cdot (H\nu\boldsymbol{\nabla}\bar{\mathbf{u}}) + \frac{\tau^s - \tau^b}{\rho H} + \boldsymbol{\nabla}U \tag{2.7}$$

To summarize, the unmodified SWE read :

$$\begin{cases} \frac{\partial \mathbf{u}}{\partial t} + \mathbf{u} \cdot \boldsymbol{\nabla}\mathbf{u} + f\mathbf{e}_z \wedge \mathbf{u} + g\boldsymbol{\nabla}\eta = \frac{1}{H}\boldsymbol{\nabla} \cdot (H\nu\boldsymbol{\nabla}\mathbf{u}) + \frac{\boldsymbol{\tau}^s - \boldsymbol{\tau}^b}{\rho H} + \boldsymbol{\nabla}U \\ \frac{\partial \eta}{\partial t} + \boldsymbol{\nabla} \cdot (H\mathbf{u}) = 0 \end{cases} \tag{2.8}$$

with

$\frac{\partial \mathbf{u}}{\partial t}$ : local acceleration

$\mathbf{u} \cdot \boldsymbol{\nabla} \mathbf{u}$ : convection

$f \mathbf{e}_z \wedge \mathbf{u}$ : Coriolis force

$g \boldsymbol{\nabla} \eta$ : gradient of free surface

$\frac{1}{H} \boldsymbol{\nabla} \cdot (H \nu \boldsymbol{\nabla} \mathbf{u})$ : diffusion

$\frac{\boldsymbol{\tau}^s - \boldsymbol{\tau}^b}{\rho H}$ : constrain at the surface and the friction of the bottom

$\boldsymbol{\nabla} U$ : forcing of Saturn due to the gravity

### 2.2.3 Adapted hydrodynamic model

Considering that the deformations of the ice shell define the sea surface elevation is a good way to take into account the ice shell above the GSO. Besides, it must be mentioned that this is similar to the rigid lid approximation. To apply this to the sea elevation, the SWE have to be adapted. Indeed, $\eta$ is no longer an unknown variable while the surface pressure is now one.

The modified SWE then change into a system of three equations ( 2 momentum equations + 1 continuity equations) with three unknowns ($u_x$, $u_y$, $p_s$ ) :

$$\begin{cases} \frac{\partial \mathbf{u}}{\partial t} + \mathbf{u} \cdot \boldsymbol{\nabla} \mathbf{u} + f \mathbf{e}_z \wedge \mathbf{u} + g \boldsymbol{\nabla} \eta + \frac{1}{\rho} \boldsymbol{\nabla} p_s = \frac{1}{H} \boldsymbol{\nabla} \cdot (H \nu \boldsymbol{\nabla} \mathbf{u}) + \frac{\boldsymbol{\tau}^s - \boldsymbol{\tau}^b}{\rho H} + \boldsymbol{\nabla} U \\ \frac{\partial \eta}{\partial t} + \boldsymbol{\nabla} \cdot (H \mathbf{u}) = 0 \end{cases} \tag{2.9}$$

because

- $\eta$ being a known variable so is $\frac{\partial \eta}{\partial t}$. Therefore, the latter becomes a source term.
- the surface pressure becomes the third unknown instead of the sea surface elevation in the momentum equations.

Besides, two terms of numerical stabilization are added $\epsilon_s \frac{H}{\rho} \Delta p_s$ and $\epsilon_t \frac{H}{\rho} \frac{\partial p_s}{\partial t}$ to the continuity equation. These terms represent a pseudo-compressibility which facilitates the stabilization of the results. The first one is a spatial relaxation term with a spatial relaxation factor $\epsilon_s$. The second one is a relaxed temporal variation of the pressure. Therefore, the continuity equation reads :

$$\epsilon_t \frac{H}{\rho} \frac{\partial p}{\partial t} \frac{\partial \eta}{\partial t} + \boldsymbol{\nabla} \cdot (H \mathbf{u}) + \epsilon_s \frac{H}{\rho} \Delta p_s = 0$$

#### Sea elevation model

First of all, before obtaining the results, I have to take a reference case. Consequently, my first case of study will be to consider that there is no icy surface above the GSO. This hypothesis is equivalent to considering that crust is an elastic ice shell. It will

deform just like to the ocean. Hence, its impact is limited to an additional friction term related to the upper ocean boundary.

$$\eta = free \tag{2.10}$$

I will now describe the models that will be studied to simulate the flow. For the modified model, I will consider that the tides are generated by a tidal potential due to Saturn[Beu15b] :

$$\eta = \frac{h_2}{g} U(r = R) \tag{2.11}$$

with

U : tidal potential

$h_2$ : radial tidal love number (which can be complex depending on the rheology)

R : mean radius

# Chapter 3

# Results of the free surface

In this section, I will describe and analyze the results obtained for the free surface case. The reference depth will be 10km. I choose this depth as reference because the results were among the simplest and less complex. Moreover, its elevation seems to be the more recurrent among all the elevation.

## 3.1 Reference case

### 3.1.1 The elevation

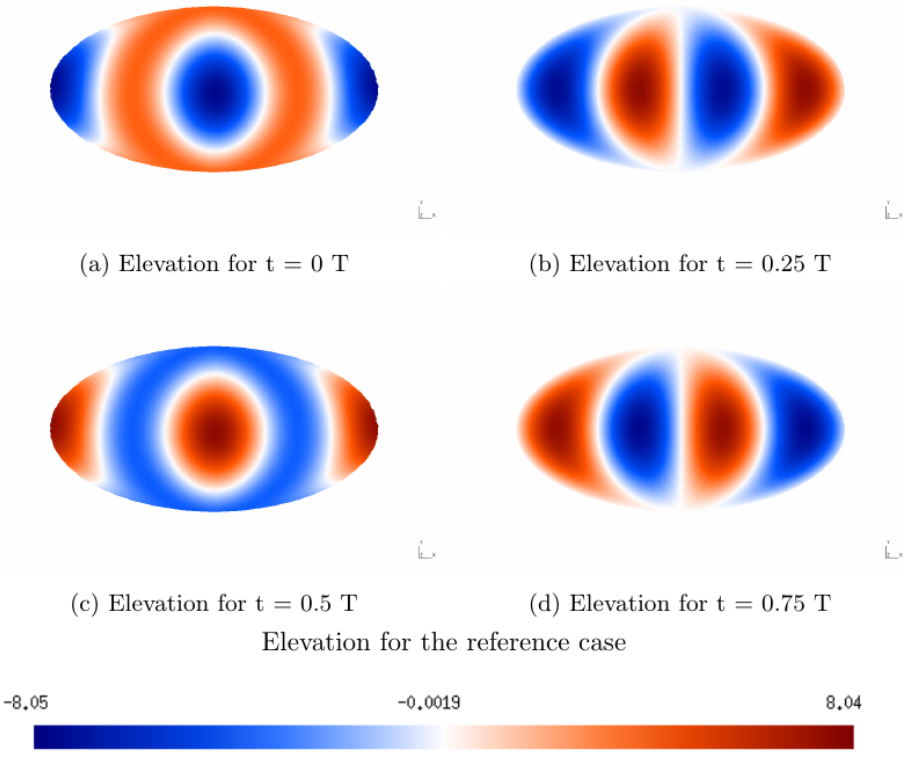


(a) Elevation for t = 0 T

(b) Elevation for t = 0.25 T

(c) Elevation for t = 0.5 T

(d) Elevation for t = 0.75 T

Elevation for the reference case

FIGURE 3.1: Elevation of the reference case [m]

On figure 3.1, the elevation of the GSO for a depth of 10km is represented for four moments of a Titan day, T representing the total duration of a Titan day. The amplitude of the tides goes from -8.05m to 8.04m. At the beginning of the period, the high tides are located at a ring passing through the two poles while the low tides are located at two opposite circular regions centered at the equator of Titan, which

formed two tidal bulges. Each of them crosses the half of Titan over one period. The tidal bulges move around until the GSO is perfectly divided into 4 parts alternating high tides and low tides. Finally, they move again around and restart the previous moves by reversing their place. One can see that through the day, the tidal responses are symmetric, the figure at t = 0 T is symmetric to t = 0.5T. This is the same for the two others figures.

### 3.1.2 The two components of the velocity

In this section, I will describe and analyze the components of the velocity of the GSO for a depth of 10000m. To show the longitudinal and latitudinal velocity, I will use three different views. The system of axes of each view is represented on figure 3.2. This system will be used for representing others variables like the velocity field. Furthermore, on figure 3.3 , the system of axes for the spheric coordinates is represented.

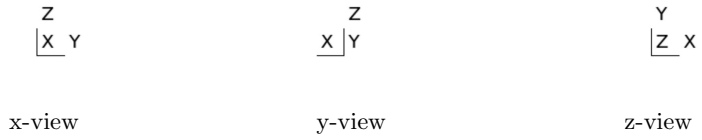


FIGURE 3.2: System of axis of each view

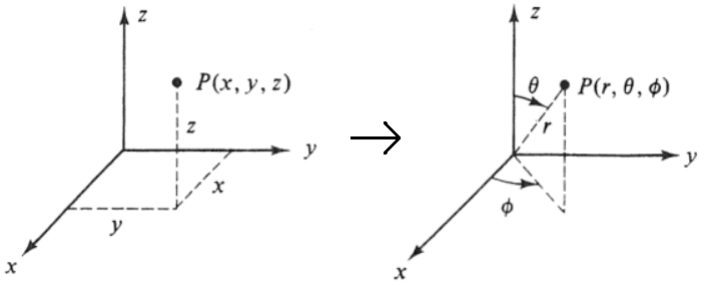


FIGURE 3.3: System of axis for the spheric coordinates

One can see the representation of the longitudinal velocity for two instants on figure 3.4. The speed of the longitudinal velocity of the GSO for a depth of 10000m goes from -0.0116m$s^{-1}$ to 0.0117m$s^{-1}$. Like the elevation, the longitudinal velocity is symmetric throughout a period. Moreover, the maximum and the minimum values do not change significantly through the period. For t = 0T, the GSO is divided into three regions. Two regions are composed of tides with a positive longitudinal velocity while the last region is composed of tides with a negative one. The two first regions are circular areas centered at points with latitude of $\frac{\pi}{4}$ and $\frac{3\pi}{4}$. For 0.25 T, the GSO is divided into four regions of same size alternating positive and negative velocities.

Concerning the latitude velocity, the speed goes from -0.0113m$s^{-1}$ to 0.0113m$s^{-1}$. Like the longitudinal velocity, it is symmetric and the extrema do not change significantly with the time. For t = 0T and t = 0.25T, the GSO is divided into six regions alternating positive and negative velocities. On figure 3.5, one can see the latitude velocity. Contrary to the previous velocity, its configuration stays the same during all the period. the configuration just turns around a rotation axis passing through the two poles.

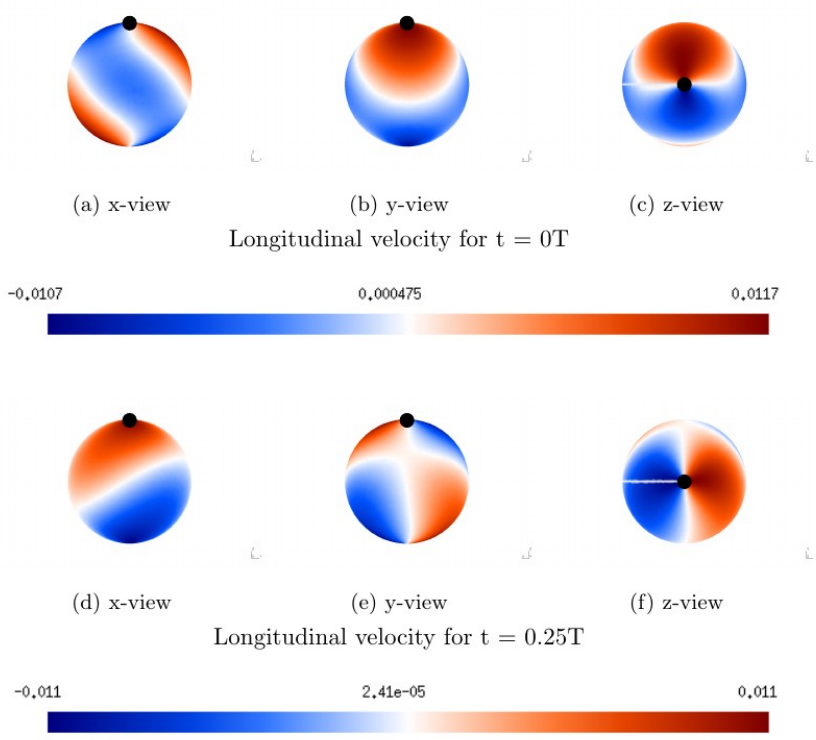


FIGURE 3.4: Longitudinal velocity of h = 10000m
The black dot represents the North Pole

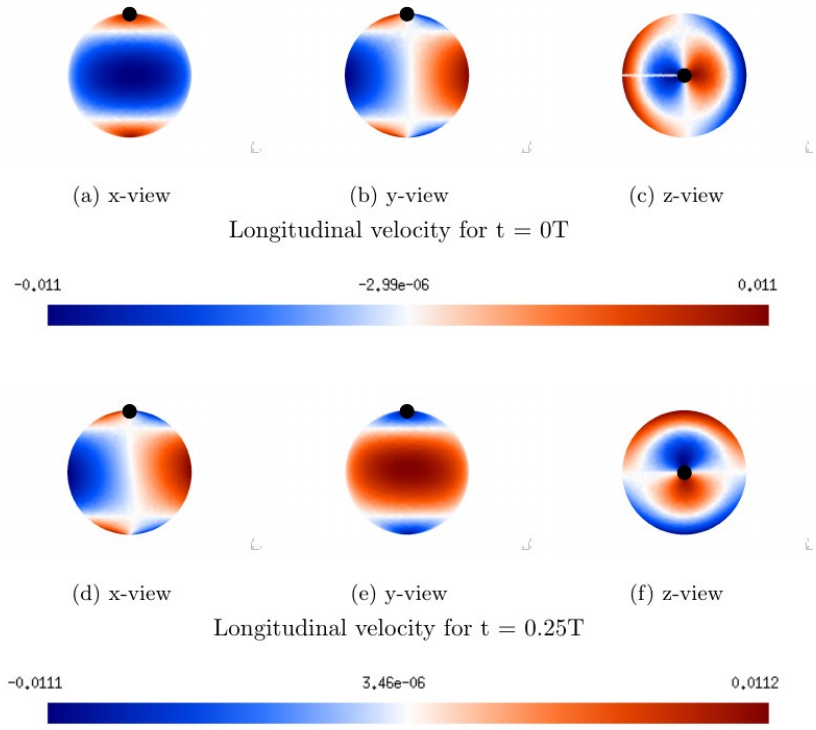


FIGURE 3.5: Latitudinal velocity of h = 10000m

### 3.1.3 The Velocity field

Finally, to have a better view of the velocity, on figure 3.6, one can see the velocity fields for three different views and two different times of the period. I choose only two times because the two others are simply symmetric.

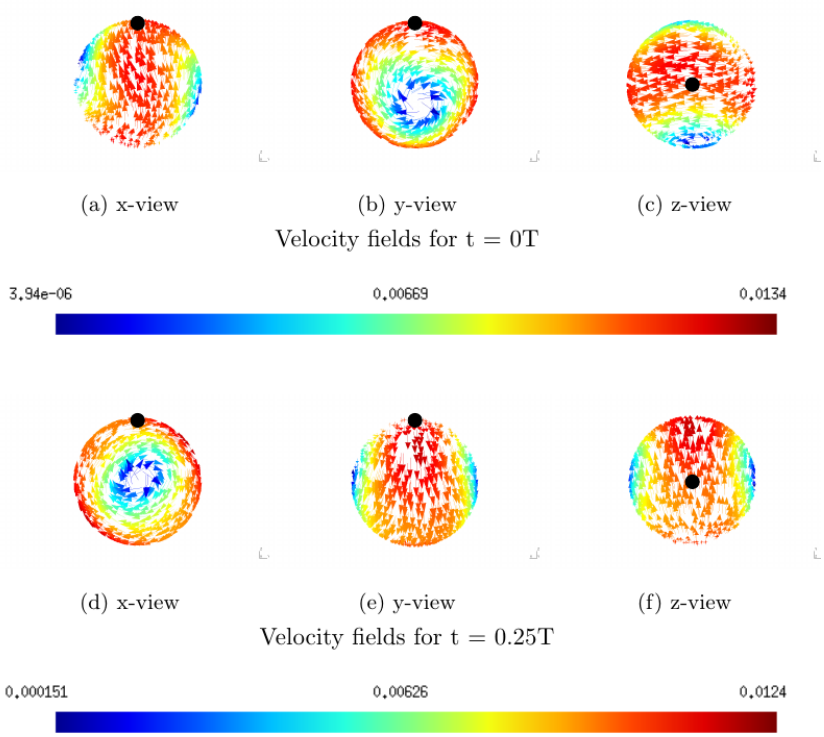


FIGURE 3.6: Velocity field of the reference case [$ms^{-1}$]
The black dot represents the North Pole

One can see that the areas where the speed is the lowest are two circles centered at the equator of Titan. Then, the area of the maximum speed is a ring going through the two poles. The figure also shows that the arrows seem to turn around a rotation axis passing through the two circles with the lowest speed. During the whole period, this configuration just turns around the axis of symmetric passing through the poles of the moon. Moreover, it is interesting to see that for t = 0 T and t = 0.25 T, the x-view and the y-view are quite the same. By that , I mean that the x-view of t = 0T is more or less the same that the y-view of t = 0.25 T. The conclusion I can make is that the velocity fields seems to always have the same configuration all along the period. The regions with the high speed and the regions with the low speed seem to always have the same form. Eventually, the extrema of the norm of the velocity are 0 $ms^{-1}$ and 0.0134 $ms^{-1}$.

For the analysis of the others depths' velocities, only the representation of the velocity field will be shown and compared.

## 3.2 The others depths

### 3.2.1 The elevation

One can see the extrema of each tides on the table 3.1. I have made a interpolation with cubic splines to see the function of the elevation on the figure 3.7. Nevertheless,

| Depth (m) | 50 | 100 | 500 | 1000 | 5000 | 10 000 | 50 000 | 100 000 |
|---|---|---|---|---|---|---|---|---|
| Amplitude max (m) | 6.98 | 9.95 | 8.4 | 8.81 | **12.3** | 8.04 | 8.33 | 7.43 |
| Amplitude min (m) | -6.41 | -10 | -8.38 | -8.53 | **-12.1** | -8.05 | -8.64 | -7.43 |

TABLE 3.1: Maximum and minimum elevation of each depths

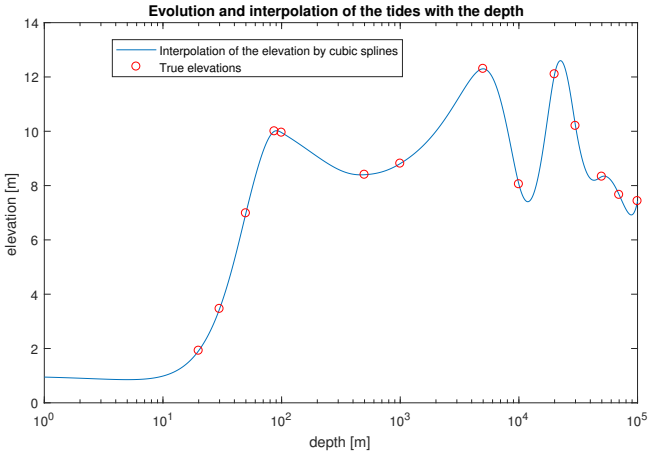


FIGURE 3.7: Interpolation of the elevation in function of the depth

the interpolation does not looks very good. Indeed, for some depth, the elevation is negative. This interpolation is bad probably because the depths are too distant (e.g. 100m and 50.000m).

The maximum values of the elevation are all close to $\pm 10m$. The smallest ones appear with a depth of 50m and the highest ones, which are almost the double, appear for 5000m. Visually, the tides, which appear at 500m, 1000m and 100.000m, behave the same way than the tides of 10.000m. It means that the tides moves following the same pattern.

However, for the depths of 50m and the 100m, phase shifts with respect to the depth of 10.000m appear. The two phase shifts can be observed in the figures 3.8 and 3.9. The former case suffers a bigger phase shift. This can be explained by the configuration of Titan for these depths. The depth of the GSO is really small in comparison of the thickness of the layers above and below it. From a relative point of view, these depths are only 1% of the thickness of the others layers. The thickness of these layers is about 100km. Then, a GSO with a depth of 100m could generate a phase shift. I assume that the elevation for others small depths should also have a phase shift.

The elevation for the depths 5000m and 50.000m seems to have some interesting behaviors. They both suffer greatly the effect of many frequencies. On the figures 3.10 and 3.11, one can see the elevation of these two depths for a few consecutive time steps. In contrary to the reference case, the elevations change a lot in a really short time. This effect is what I mean when I say they both suffer the effect of many frequencies. A way to explain that is to look at the components of the tides.

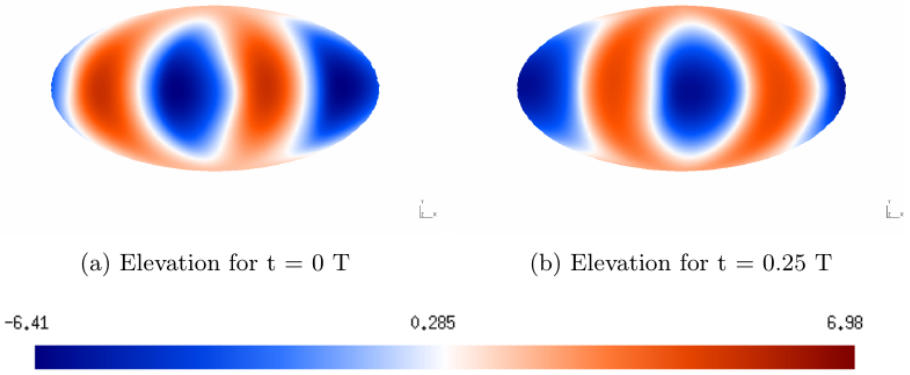


(a) Elevation for t = 0 T (b) Elevation for t = 0.25 T

FIGURE 3.8: Elevation of h = 50m [m]

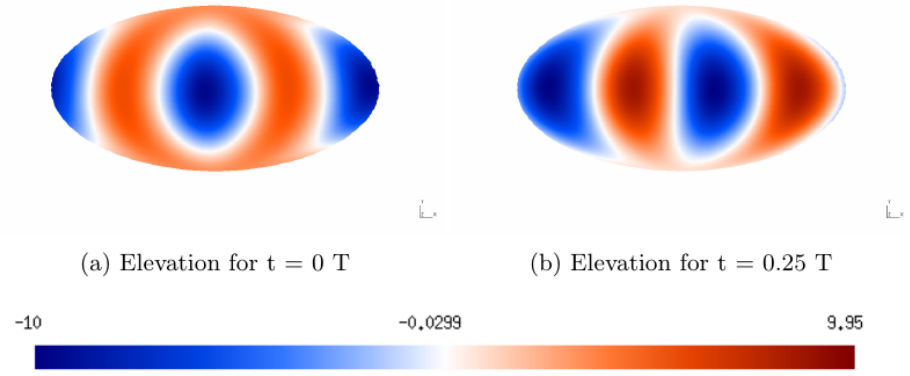


(a) Elevation for t = 0 T (b) Elevation for t = 0.25 T

FIGURE 3.9: Elevation of h = 100m [m]

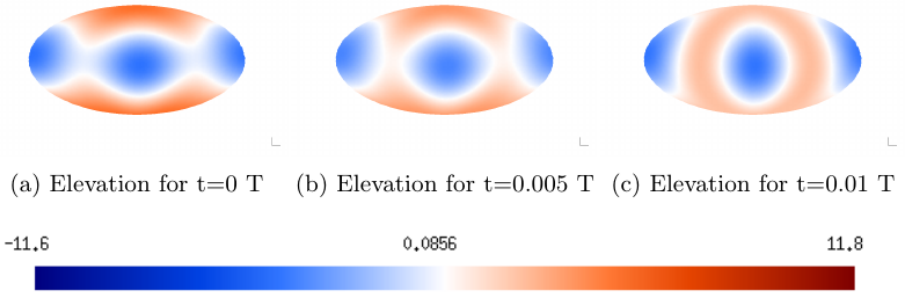


(a) Elevation for t=0 T (b) Elevation for t=0.005 T (c) Elevation for t=0.01 T

FIGURE 3.10: Elevation for h = 5000m for a few steps [m]

To avoid misunderstanding, let's make the definition of the $i^{th}$ component. The $i^{th}$ component of the tides is defined by the following frequency :

$$\omega^{i^{th}} = \frac{2\pi}{T/i} = \frac{2\pi i}{T}$$

Normally, by taking a Titan day as the reference period, the main tidal component should be the first one. Then, the importance of the others one should be small. If this

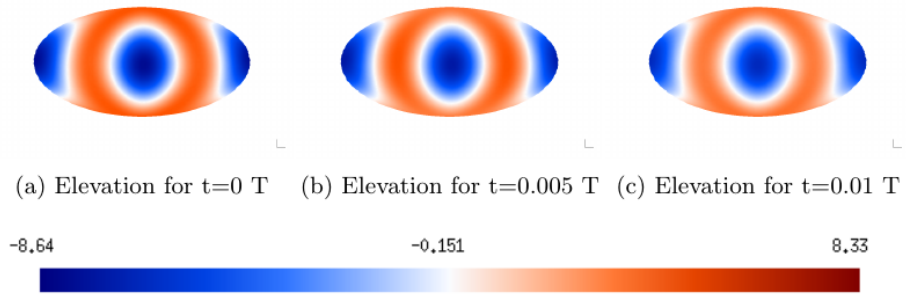


(a) Elevation for t=0 T (b) Elevation for t=0.005 T (c) Elevation for t=0.01 T

FIGURE 3.11: Elevation of h = 50.000m for a few steps [m]

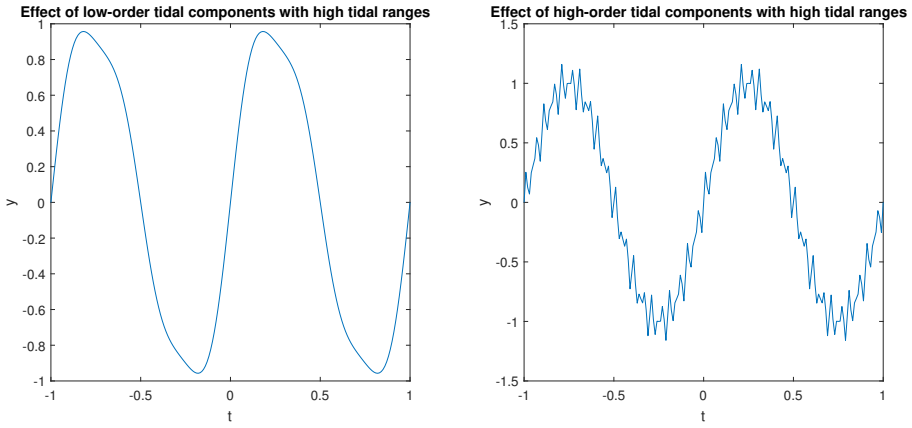


FIGURE 3.12: Comparison of the effect of low-order and high-order tidal components

is not the case, it would mean that resonances or interferences appear. If the resonance appears for high-order frequencies or, in others words, for high components, the effect is that the sum of the component will oscillates a lot. On figure 3.12, you can see this phenomena. The first graph represents the case where the first, the second and the third component are important. The second graph represent the case where the first, the twentieth and the thirtieth component are important. Of course, I give the same weights to the extra components for the two cases.

For 5000m, the component with high-order frequencies seem to have a big importance. For the second case, components with very high frequencies seems to be significant. They have probably frequencies bigger than the previous case. I suggest that because the general movement follows a frequency of $\frac{2\pi}{T}$ like the reference case while the region of high tides and low tides oscillate a lot.

### 3.2.2 The Principal tidal components

To validate my hypothesis, I will show the principal components of the tides for each depths. To be sure to not miss any important ones, I checked until the $100^{th}$ component.

On figures 3.13 , one can see the three principal components of the tides for h = 50m, 100m, 500m, 10.000m and 100.000m. For these depths, the first component is by far the bigger. They are followed by components up to fifth one. However,

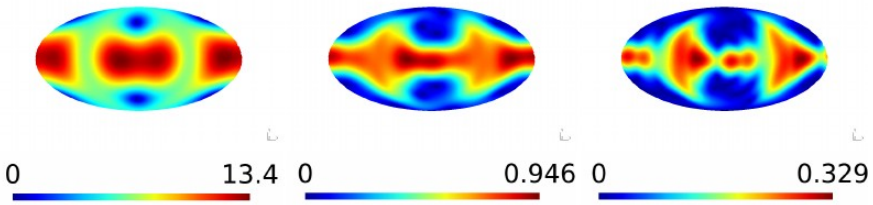


(a) $1^{st}$ component (b) $3^{rd}$ component (c) $5^{th}$ component

Principal component of the tides for h = 50m

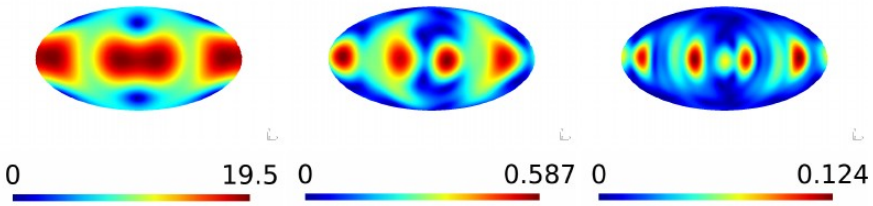


(a) $1^{st}$ component (b) $3^{rd}$ component (c) $5^{th}$ component

Principal component of the tides for h = 100m

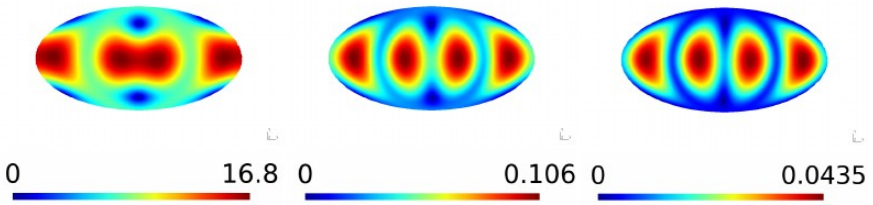


(a) $1^{st}$ component (b) $2^{nd}$ component (c) $4^{th}$ component

Principal component of the tides for h = 500m

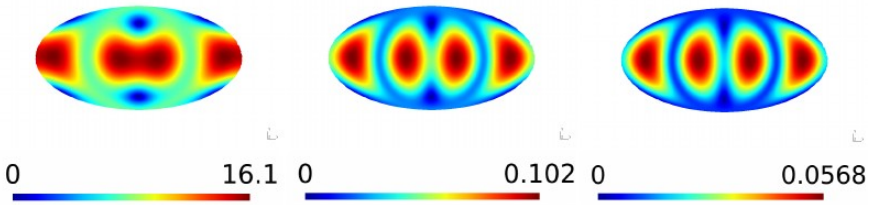


(a) $1^{st}$ component (b) $2^{nd}$ component (c) $3^{rd}$ component

Principal component of the tides for h = 10.000m

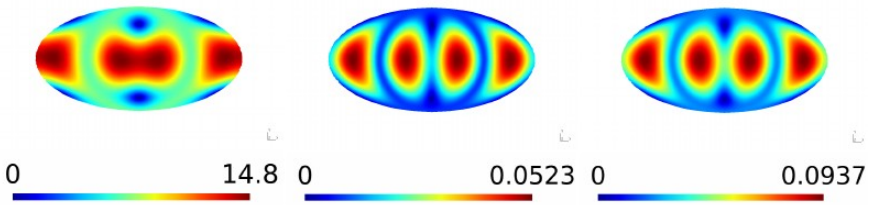


(a) $1^{st}$ component (b) $3^{rd}$ component (c) $2^{nd}$ component

Principal component of the tides for h = 100.000m

FIGURE 3.13: Normal principal components

the amplitudes are not big at all. The others ones are really small. One can say that they are insignificant in comparison. These results match with the previous section. Indeed, the elevation of their tides follow mainly one frequency.

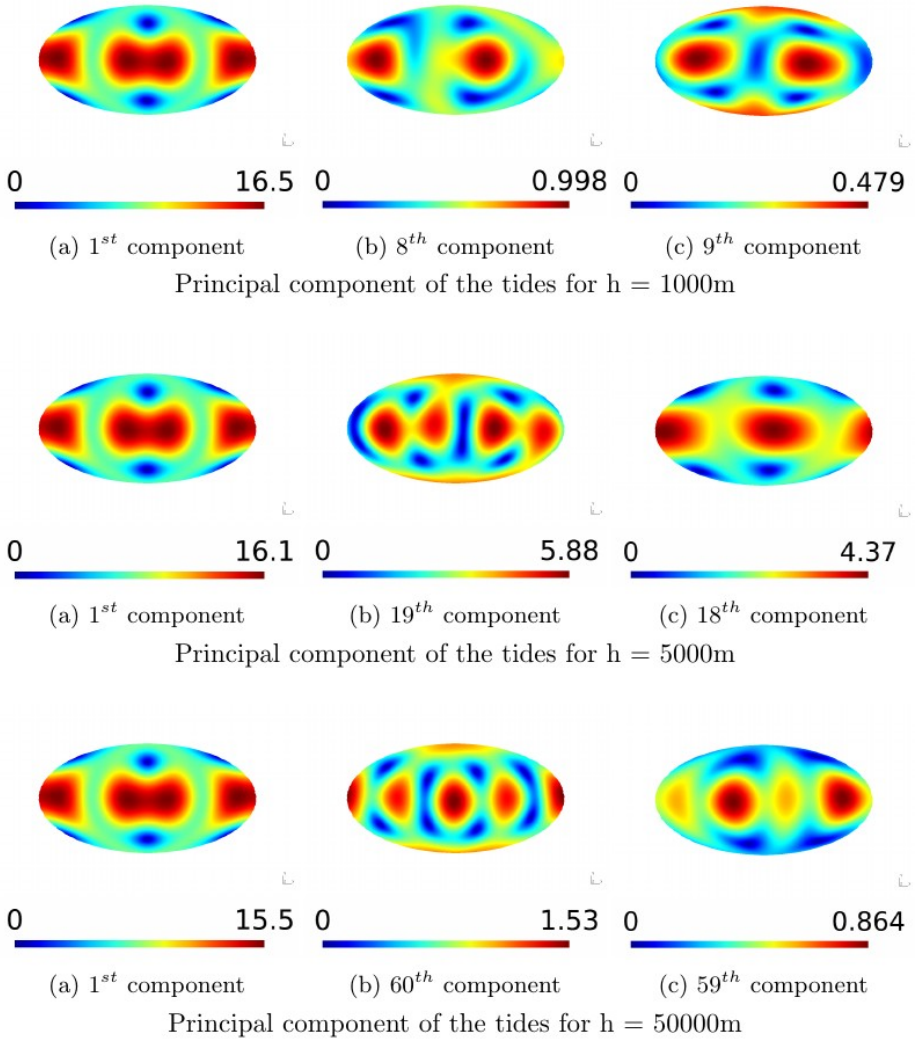


(a) $1^{st}$ component (b) $8^{th}$ component (c) $9^{th}$ component

Principal component of the tides for h = 1000m

(a) $1^{st}$ component (b) $19^{th}$ component (c) $18^{th}$ component

Principal component of the tides for h = 5000m

(a) $1^{st}$ component (b) $60^{th}$ component (c) $59^{th}$ component

Principal component of the tides for h = 50000m

FIGURE 3.14: Special principal components

Furthermore, on figure 3.14, the principal component for 1.000m, 5.000m and 50.000m can be seen. In the previous case, the first component is the principal one. However, as expected, the second and third principal components tend to have high frequencies. For h = 1.000m, the $8^{th}$ and the $9^{th}$ component follow the first one. This explains the behavior of the velocity fields.

For h = 5.000m, the $19^{th}$ and the $18^{th}$ ones follow the first one. They have very high amplitudes. Indeed, they represent more or less respectively 23% and 15% of the amplitude of the tides. This matches quite well with the behavior of the elevation..

For h = 50.000, even higher component appear at the second and third places. They are the $56^{th}$ and the $55^{th}$ ones. However, their amplitudes are not as impressive as the one for h = 5.000m. This also matches with the results obtained for the elevations of the tides.

### 3.2.3 The Velocity fields

| Depth (m) | 50 | 100 | 500 | 1000 | 5000 | 10 000 | 50 000 | 100 000 |
|---|---|---|---|---|---|---|---|---|
| $\|v\|$ (m/s) | **0.438** | 0.372 | 0.0847 | 0.07 | 0.0522 | 0.0134 | 0.0174 | 0.00134 |

TABLE 3.2: Velocities maximum and minimum

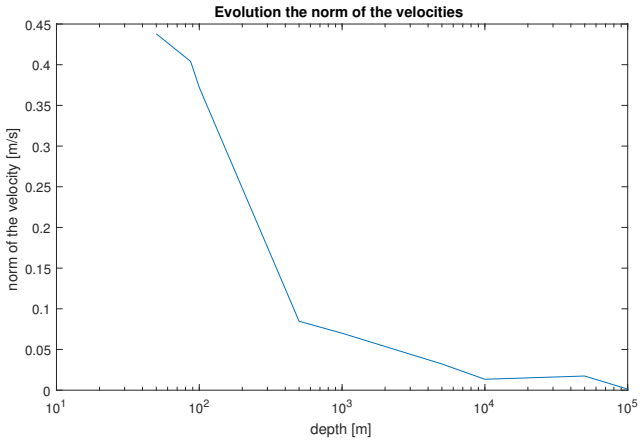


FIGURE 3.15: Velocities in function of the depth

On the table 3.2, one can see the different velocities extrema. To have a better idea of these results, one can see on figure 3.15 the evolution of the norm of the velocity. This time, the tides for a depth of 50m have the bigger extrema. Actually, these values decrease as the depth increases except for h = 50000. Compared to the smallest ones which appear for 100km, the ratio is 400. Such a ratio is quite impressive and big. The behavior of the velocity fields follow globally the same pattern of the behavior of the elevation. It means that for the depths 5000m and 50.000m, they vibrate a lot. Furthermore, for 1000m, the velocity also seems to vibrate. This is interesting because the elevation doesn't have this pattern.

For the other cases, the fields are either the same as the reference case or have a phase shift. For instance, for 100000m, the velocity is quite the same while, for 100m, it has a phase shift.

Now, let's take a look at the velocity fields' figures.

For the depth on figure 3.16, the lowest speeds are also located at circles centered at the equator. However, a thin ring going through the pole also have the lowest speeds. The thickness of this ring changes through the period. It grows until 0.5 T then decreases until the 1T.

For the depth of 100m, the areas of the minimum speed is composed of two rings going through the poles. Consequently, the maximum values are located at four zones. As the previous depth, one rings grows and decreases through the period.

For the next depths, the representations of their velocity field became to difficult to describe. Therefore, I will show them together and briefly compare them.

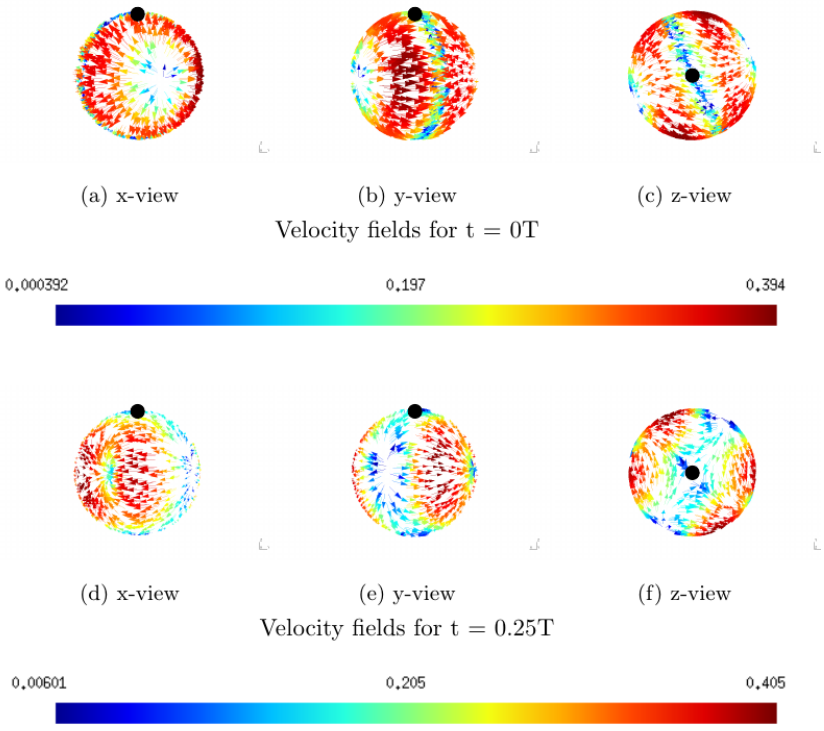


FIGURE 3.16: Velocity field for h = 50m [$ms^{-1}$]

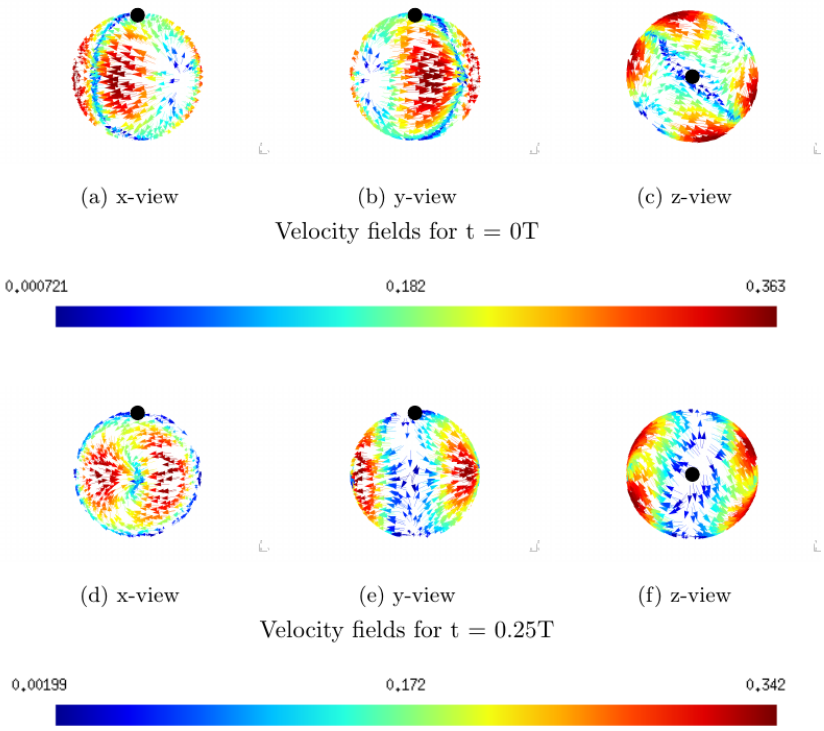


FIGURE 3.17: Velocity field for h = 100m [$ms^{-1}$]

On the figures from 3.18 to 3.21, one can see that the areas with the minimum speeds are globally bigger than the area with the maximum ones. They both moves around the axis of symmetric with the time.

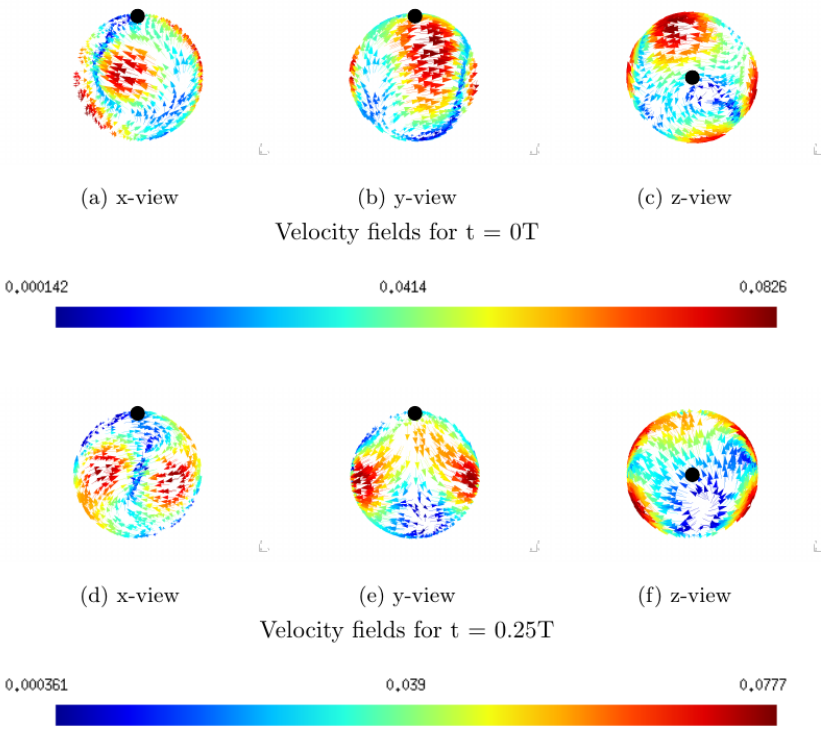


FIGURE 3.18: Velocity field for h = 500m [$ms^{-1}$]

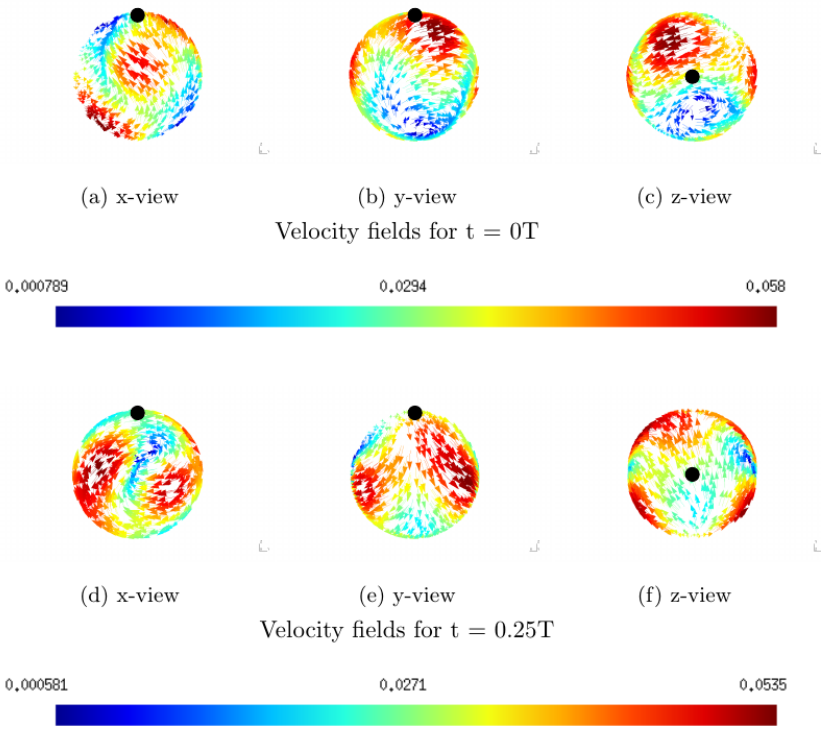


FIGURE 3.19: Velocity field for h = 1000m [$ms^{-1}$]

On figure 3.22, the last depth is represented. The behavior is the same as reference case.

Finally, there is a special depth that I have studied and analyzed. This depth

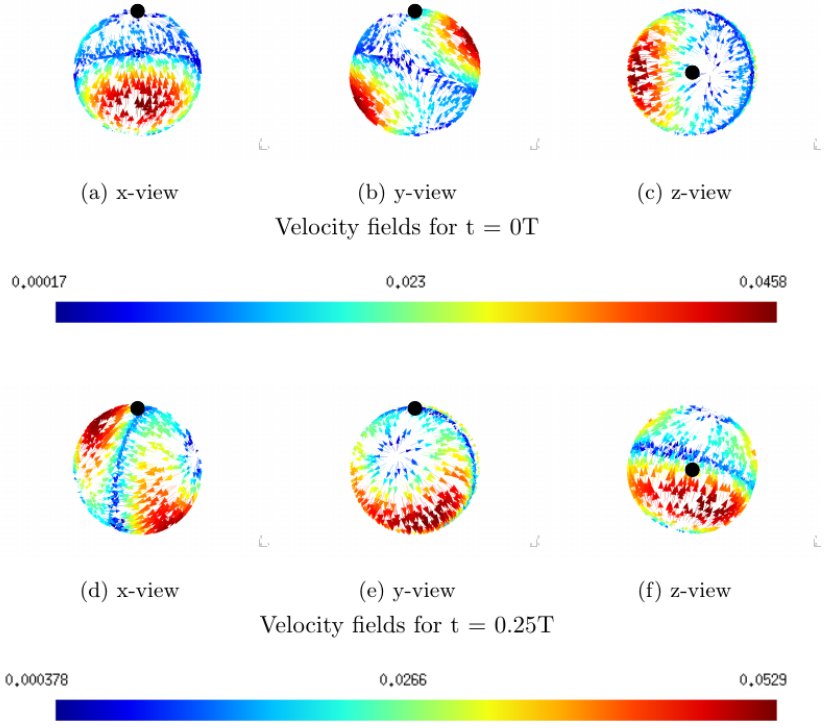


(a) x-view (b) y-view (c) z-view

Velocity fields for t = 0T

(d) x-view (e) y-view (f) z-view

Velocity fields for t = 0.25T

FIGURE 3.20: Velocity field for h = 5000m [$ms^{-1}$]

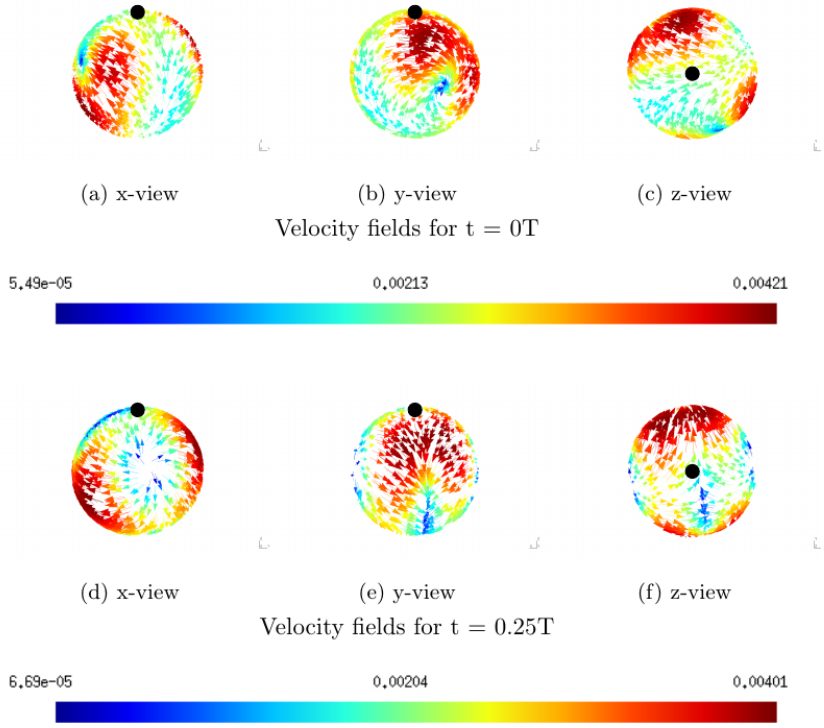


(a) x-view (b) y-view (c) z-view

Velocity fields for t = 0T

(d) x-view (e) y-view (f) z-view

Velocity fields for t = 0.25T

FIGURE 3.21: Velocity field for h = 50000m [$ms^{-1}$]

whose the characteristic speed is the same than the rotation speed of Titan. Having

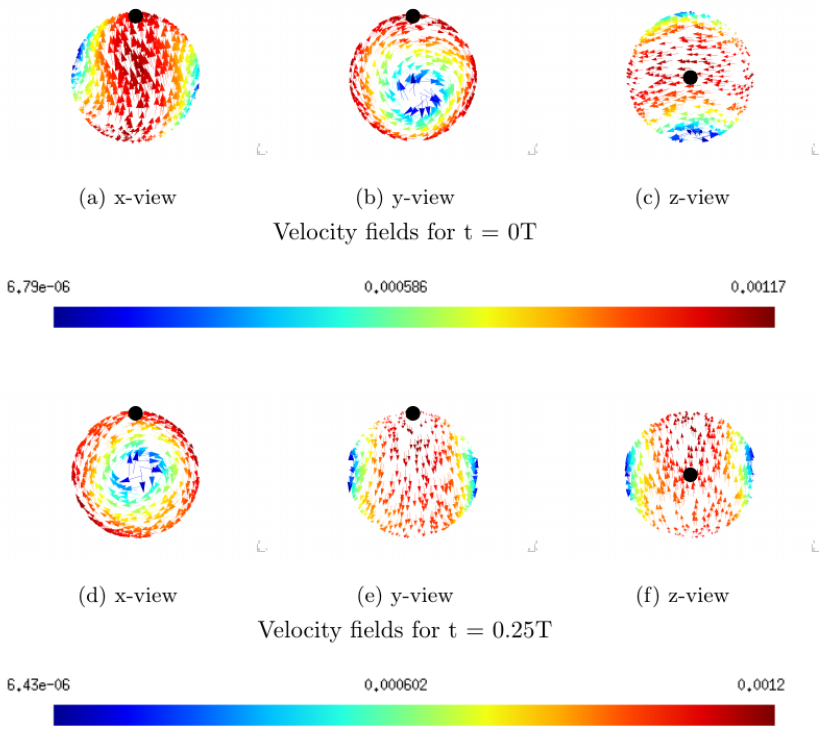


FIGURE 3.22: Velocity field for h = 100000m [$ms^{-1}$]

this specificity, I hoped that the results could be interesting.

$$\sqrt{gh} = \frac{2\pi R}{T}$$

This values is 87,44627906m. The maximum and minimum amplitude are $\pm 10m$. The extrema of the three components of the velocity are $\pm 0.404$, $\pm 0.403$ and $\pm 0.225$. These values do not stand out. Furthermore, the visual results were pretty close to the one obtain for 50m. Unfortunately, they have not particular characteristics.

## 3.3 Summary

The two previous sections showed interesting results. For most of the depths, the elevation is influenced only by one tidal component. The behavior of the tides then follows the same pattern. The notable differences were the amplitude of the elevation and the phase shift. However, the extrema of the tides were always close to $10m$. For some depth, high-order components influence the elevation. The effects were that the regions of the high and the low tides vibrate or change a lot through time. Furthermore, the depth changes also the velocity field. This latter can be very different from one depth to the others.

After analyzing the elevation and the velocity of the tidal flow for different ocean depths, an obvious conclusion can be made. The ocean depth has a significant impact on the tidal flow and the tidal component. However, for each depth, the first tidal component remain the same.

# Chapter 4

# Results of the tidal potential

## 4.1 The Love number

As I introduced it earlier, one way to take into account the crust above the global subsurface ocean is to assume that the motion of the ice shell at the top of the ocean is given by

$$\begin{aligned}\eta &= \frac{h_2}{g} U(r = R) \\ &= \frac{h_{2r} + i h_{2i}}{g} U(r = R)\end{aligned}$$

where $U$ is the tidal potential due to Saturn and $h_2 = h_{2r} + i h_{2i}$ is the radial Love number. Moreover, in this model, the ocean has a feedback from the solid layer but not the other way around. The principal difficulty is then to determine the value of the radial Love number $h_2$. There are theoretical formulas to express this number. However, these formulas would take too long to apply. Consequently, I looked for a potential value in the literature and I found two proper articles[Beu15a][FSL03]. They do not give a precise value but give instead a range for the value of $h_2$.

### 4.1.1 First range

In the first article, the density of the model is separated into three categories in function of the density of the ocean and the crust : light, mixed and dense.

| Density model | Ocean $\bar{\rho}\ [\frac{kg}{m}]$ | Crust $\rho\ [\frac{kg}{m}]$ | Contrast $\frac{\delta\rho}{\rho}$ |
|---|---|---|---|
| Light | 930 | 1020 | -0.9 |
| Mixed | 930 | 1280 | -0.27 |
| Dense | 1167 | 1280 | -0.9 |

TABLE 4.1: Density models for the crust and the ocean of Europa and Titan
credit : [Beu15a]

In function of these densities, the range for the Love number changes. Choosing the right category is important. Considering the characteristics of Titan described earlier, the right density is the Light density. Indeed, the density of the ocean and the crust are respectively 1023.5 $kgm^{-1}$ and 930.8 $kgm^{-1}$. It gives then a contrast of $-0.9$. Knowing that, the range of the real part of the Love number can be found

on the figure 4.1 in function of the ratio between the thickness of the crust and the height of the crust-ocean boundary . This ratio is called the relative crust thickness.

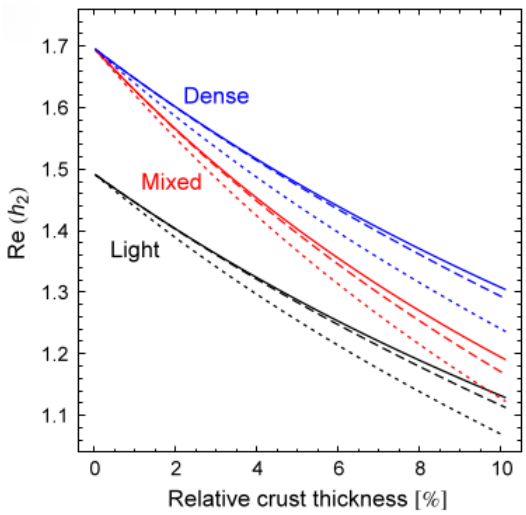


FIGURE 4.1: Real part of the Love number in function of the relative crust thickness
credit : [Beu15a]

Depending on the depth of the ocean, the value of this parameter goes from 0% (not included of course) to 10%. One can see that the range of $Re(h_2)$ for the Light case goes from 1.5 to 1.1. Unfortunately, the imaginary part of the Love number for Titan is expressed by too complex mathematical formulas. Nevertheless, the article gives the range of the norm of the Love number of Europa. One can see the graph on the figure 4.2. Europa is a icy moon of Jupiter presented in the chapter 2 on the figure

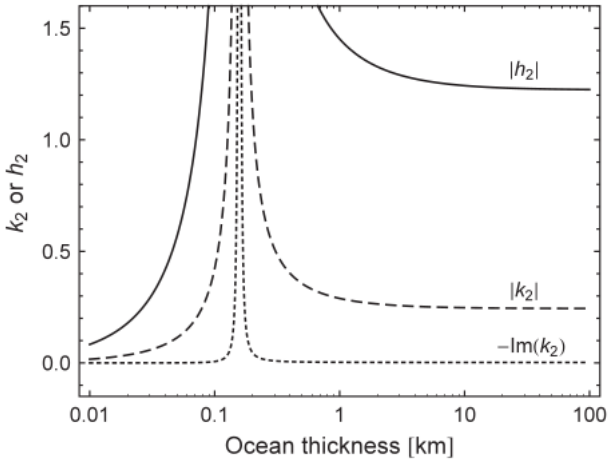


FIGURE 4.2: Norm of the Love number of Europa in function of the ocean thickness
credit : [Beu15a]

2.2. It has many things in common with Titan. For instance, a global ocean is present under the crust, Europa is tidally locked in synchronous rotation with Jupiter and its gravity and its surface temperature is close to the one of Titan. Therefore, I made the hypothesis that I can rely on the norm of the Love number of Europa to predict Titan's.

### 4.1.2 Second range

In the second article, the model of Titan is separated in two in function of the composition of the ocean. The ocean is composed of water and ammonia. From that, the author made two models depending on the percentage of ammonia in the GSO. The first one works for an ocean ammonia-water ocean composition of 15 wt.% $NH_3$ and the second one for a composition of 5 wt.% $NH_3$. The two graphs representing the Love number can be seen on the figures 4.3 and 4.4. For this article, the value of the Love number goes from approximatively 1.05 to 1.25 and from 1.15 to 1.27. Once

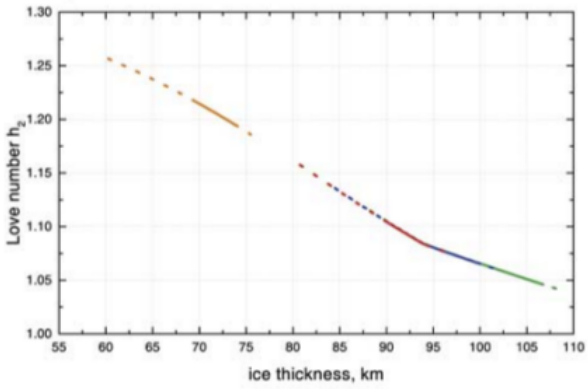


FIGURE 4.3: Real part of the Love number in function of the crust thickness
credit : [FSL03]

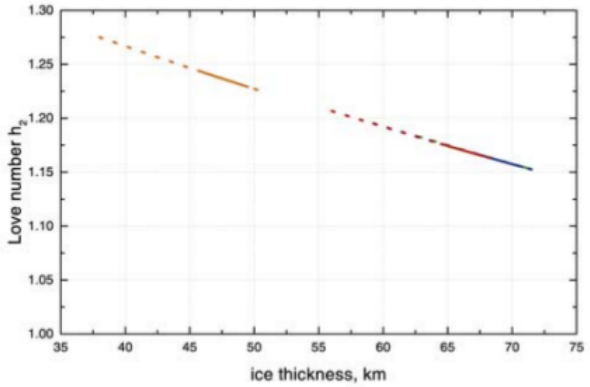


FIGURE 4.4: Real part of the Love number in function of the crust thickness
credit : [FSL03]

again, only the real part of the Love number is showed. Consequently, the norm of the Love number of Europa will again be taken into account. Unfortunately, the true value or even an approximation of the composition of the ocean is not known. Therefore, I cannot chose between the two models proposed by[FSL03]. Fortunately, the two ranges are very close to each other. Consequently, I decided to look at the mean between the real part of the two Love number of Titan.

### 4.1.3 Chosen values

Contrary to the previous chapter, the goal of this one is to study the evolution of the velocity field and the pressure in function of **the radial Love number**. As the elevation is a known variable, the pressure is the unknown variable. However, it is defined up to a constant multiplier. Therefore, the variable that has to be studied is the pressure gradient field and not the pressure itself.

To study the influence of the Love number, I can keep the same depth for each Love numbers. I decided to launch and to compare the results obtained for a depth of 10.000m. This choice was motivated by the fact that this depth was the reference case for the previous section. Furthermore, its representation of the tides was the most common one. The depth defined, I have to choose several values of the Love number based on the two articles. To have enough variety in my values without having too many values to study, I have chosen the following Love numbers :

- Real Love numbers : 1.1, 1.2, 1.3, 1.4
- Complex Love number with same imaginary part : $1.1 + 0.5i$, $1.2 + 0.5i$, $1.3 + 0.5i$, $1.4 + 0.5i$
- Complex Love number with same real part : $1.1 - 0.5i$, $1.1 + 0.15i$, $1.1 + 0.25i$, $1.1 + 0.5i$, $1.1 + 0.75i$, $1.1 + 0.85i$

The real part of these numbers stands inside the ranges proposed by the two articles. For the imaginary part, I tried to stay close to the norm showed before while not taking too complicated numbers. Thus, with these Love numbers, I will be able to study the effect of a pure real Love number and a complex Love number on the pressure gradient field and the velocity field.

## 4.2 The pressure gradient field

### 4.2.1 Pure real Love numbers

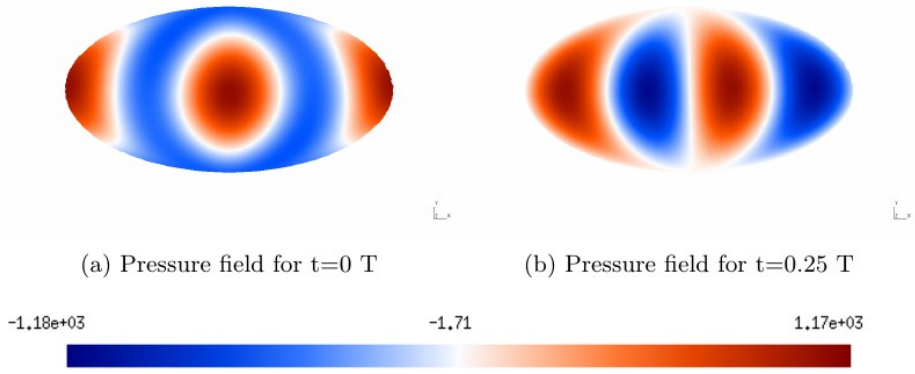


(a) Pressure field for t=0 T (b) Pressure field for t=0.25 T

FIGURE 4.5: Pressure field for $h_2 = 1.1$ [Pa]

Before talking about the pressure gradient field, I will briefly describe the pressure field and more precisely its global aspect. Despite the fact it is defined up to a constant multiplier, it is interesting to see the evolution of the pressure throughout one period T. After compiling the four real Love numbers, the four pressure fields obtained were

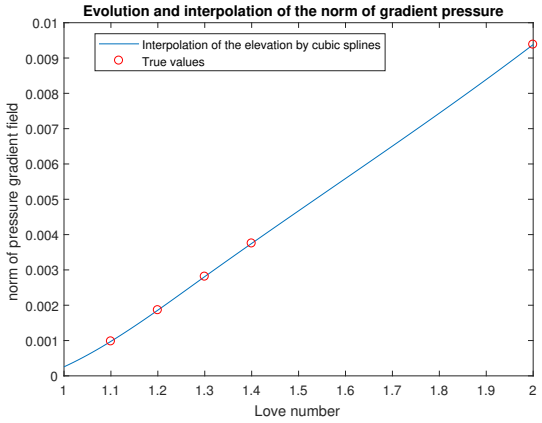


FIGURE 4.6: Interpolation of the norm of the pressure gradient field for real Love numbers

actually the same. Moreover, the results show that the pressure field follows the exact opposite behavior to the elevation. It can be seen on the figure 4.5. At the beginning of the period, the area of low and high pressure are located respectively at the same ring as the high tides and the same circular regions as the low tides. Then, it evolves into a configuration where the GSO is divided into four identical areas altering high pressure and low pressure. The next configurations are just symmetric.

This behavior of the pressure field seems coherent. Indeed, in the chapter 2, it was seen that $\boldsymbol{\nabla} p = -\boldsymbol{\nabla}\eta$. Therefore, The representation of the pressure must be the opposite of the representation of the elevation.

Let's now talk about the pressure gradient field. The first characteristic to notice is that this latter is symmetric throughout the period. Therefore, just like in the previous section, just two instants will be analyzed : t = 0T and t = 0.25T. The $T$ refers to the same $T$ as before. Moreover, the values of the extrema of $\|\boldsymbol{\nabla} p\|$ are low for every Love number. The order is $O(10^{-3})$. On the table 4.2, these values are shown. One

| Love number | 1.1 | 1.2 | 1.3 | 1.4 |
|---|---|---|---|---|
| Norm max [$10^{-3}$ Pa $m^{-1}$] | 0.977 | 1.86 | 2.81 | 3.75 |

TABLE 4.2: Maximum norm of the pressure gradient field for real Love numbers

can see that the norm grows with the Love numbers. To have an idea of the evolution of this norm for other values of the Love number, I made an interpolation by cubic splines. This can be seen in figure 4.6. To obtain this graph, I had to launched a simulation for $h_2 = 2$. The interpolation shows that the norm of the pressure gradient field follows a linear function with a slope of 0.0094. This result tends to confirm that the norm grows proportionally with the real part of the Love number.

Now that I have looked at the extrema, I will look at the behavior of the gradient fields. The first thing to say is that the representation of the field stays the same regardless of the value of the Love number. Therefore, I will only focus on one Love number, $h_2 = 1.1$. Its pressure gradient field can be seen on figure 4.7. For t = 0T, the minimum values of the norm of the pressure gradient field are located at two regions. The first one is a large ring passing by the poles. The second region is composed

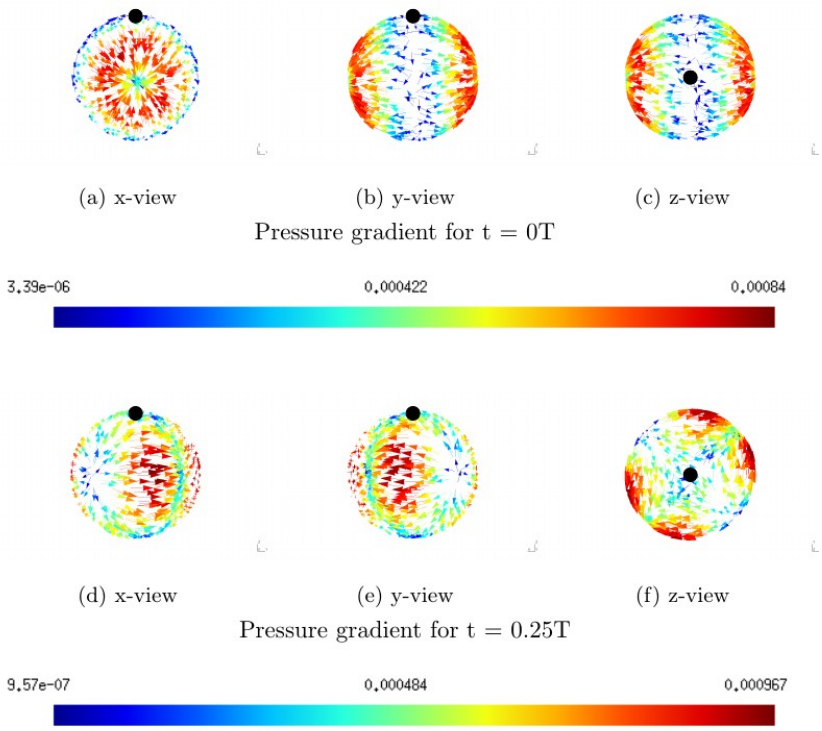


FIGURE 4.7: The pressure gradient field for $h_2$ = 1.1 [Pa]

by two little circular areas centered at the equator. The maximum values are then located between these two regions. Concerning the orientation of the arrows, it is pretty simple. They are all oriented towards the two circulars areas with low norms. To be more precise, the arrows point to the closest areas. For t = 0.25T, the minimum values of the norm are also located at two regions. A thin ring passing through the poles is the first one. Another larger ring perpendicular to the previous one is the second region. The areas of the maximum values of the norm are the four remaining regions. Concerning the direction of the arrows, they all point to the thin ring with the minimum value of the norm.

The conclusion I can make is that changing the real part of the Love number only affects the norm of the pressure gradient field and nothing else.

### 4.2.2 Complex Love numbers with the same imaginary part

Once again, the pressure gradient field is symmetric throughout the period. Furthermore, the values of the minima and the maxima of the norm are also very low. The order is again $O(10^{-3})$. The table 4.3 show the values. The maximum norms tend to

| Love number | $11 + 0.5i$ | $12 + 0.5i$ | $13 + 0.5i$ | $14 + 0.5i$ |
|---|---|---|---|---|
| Norm max [$10^{-3}$ Pa$m^{-1}$] | 4.81 | 5.12 | 5.54 | 6.67 |

TABLE 4.3: Maximum norm of the pressure gradient field for complex Love numbers with the same imaginary part

follow the same evolution as the maximum norms for the real Love numbers. They grow with the norm of the Love numbers. I made a interpolation of the maximum norm of the pressure gradient field in function of the norm of the Love number. The

graphs was almost the same as the graph on figure 4.6.

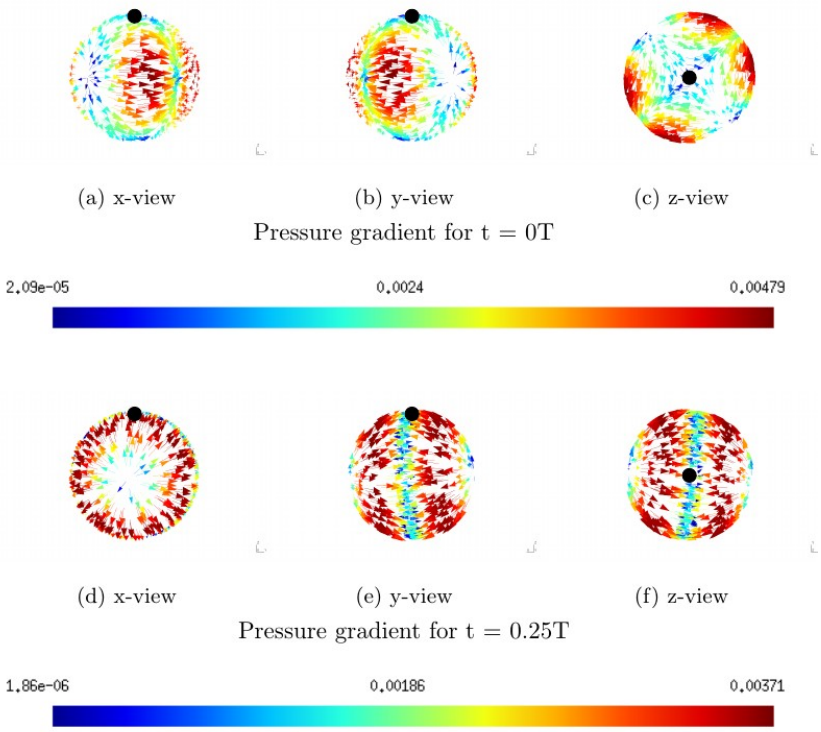


FIGURE 4.8: The pressure gradient field for $h_2$ = 1.1+0.5i [Pa]

On figure 4.8, the gradient field is shown for $h_2 = 1.1 + 0.5i$. This is the only one shown because all the others Love numbers give the same representation of the field. For t = 0T, the pressure gradient field behaves the same way as the one for $h_2 = 1.1$ and t = 0.25T. By that, I mean that the regions with the maximum and the minimum values are the same. Moreover, the arrows have the same directions. For t = 0.25T, the configuration looks just like the one for $h_2 = 1.1$ and for t = 0.25. However, the big difference is the direction of the arrows. They point in the opposite one. With all these facts, one big assumption can be made. I assume that the pressure field of $h_2 = 1.1 + 0.5i$ has the same behavior as the one of $h_2 = 1.1$ but suffers from a phase shift of $-\frac{\pi}{2}$. By checking the evolution of the pressure gradient field for the whole period for the two Love numbers, this assumption was proven to be true. The pressure gradient field of $h_2 = 1.1 + 0.5i$ is shifted compared to the one of $h_2 = 1.1$.

I can go even further in this conclusion. I assume that adding imaginary part to the real Love number in the expression of the elevation will only add a phase shift to the pressure gradient field and increase its norm. To confirm this hypothesis, I will look at the evolution of the pressure gradient field for Love numbers with the same real part. Doing so, I will even be able to know how the phase shift evolve in function of the imaginary part.

### 4.2.3 Complex Love numbers with the same real part

The values of the maximum $\|\nabla p\|$ stay quite small. They can be seen in the table 4.4. To have better understanding of the effect of the imaginary part of $h_2$, I decided

to use more values than the two previous case. This time, the maximum norms do

| Love number | $11 - 0.5i$ | $11 + 0.15i$ | $11 + 0.25i$ | $11 + 0.5i$ | $11 + 0.75i$ | $11 + 0.85i$ |
|---|---|---|---|---|---|---|
| Norm max ($10^{-3}$ Pa $m^{-1}$) | 4.84 | 1.76 | 2.6 | 4.81 | 7.17 | 8.1 |

TABLE 4.4: Maximum norm of the pressure gradient field complex Love numbers with same real part

not tend to follow the same evolution as before. Its seems that it reaches a minimum somewhere between $1.1 - 0.5i$ and $1.1 + 0.15i$. Moreover, the function describing it seems to be symmetric. The values grow for positive and negative imaginary parts of the Love number. An interpolation of this norm can be seen on the figure 4.9. The function represented is an absolute value function with its minimum at 0. This reveals that adding positive or negative imaginary part to the Love number has the same effect on the norm. Consequently, I can assume that the only difference between adding opposite imaginary part will be seen in the representation of the pressure gradient field. The sign could have an effect on the shift. It probably determines the sign of the phase shift. In others words, the sign of the imaginary part of the Love number affects the direction of the phase shift.

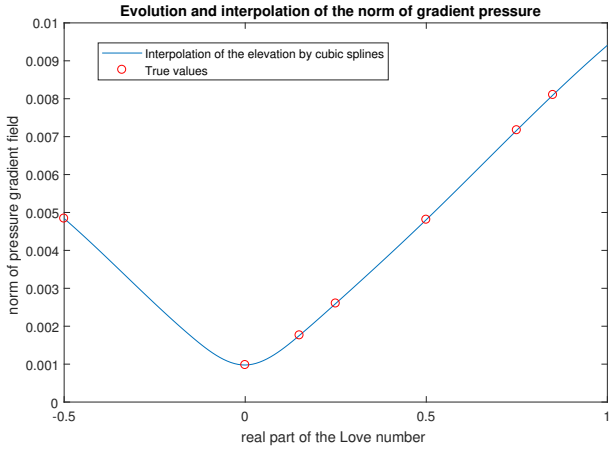


FIGURE 4.9: Interpolation of the norm of the pressure gradient field for complex Love numbers with the same imaginary part

To determine the influence of the imaginary part on the phase shift, I have launched simulation for Love numbers bigger and smaller than 0.5. Some results can be found on the figure 4.10 and 4.11. It seems that the phase shift is respectively smaller and bigger for $h_2 = 1.1 + 0.25i$ and for $h_2 = 1.1 + 0.75i$ than the one for $h_2 = 1.1 + 0.5i$. This difference can be seen by looking carefully at the North Pole. More precisely, for t = 0.25T and for the y-view, by looking at the distance between the North Pole and the ring of the minimum of the norm, one can compare the phase shift. Indeed, in comparison to $h_2 = 1.1 + 0.5i$, they seem more remote for the lowest Love number ($1.1 + 0.25i$) and closest for highest one ($1.1 + 0.75i$). I can then assume that the phase shift grows with the imaginary part of the Love number. Unfortunately, these differences in the phase shift are difficult to watch clearly. Consequently, I will show a clear comparison of the distance between the North Pole and the ring.

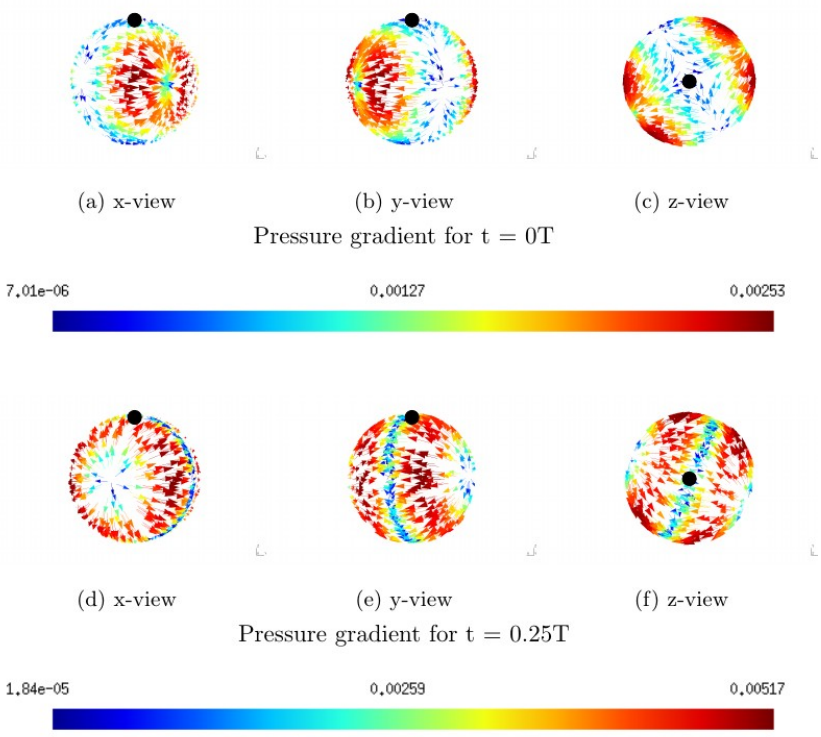


FIGURE 4.10: pressure gradient field for $h_2 = 1.1 + 0.25i$ [Pa]

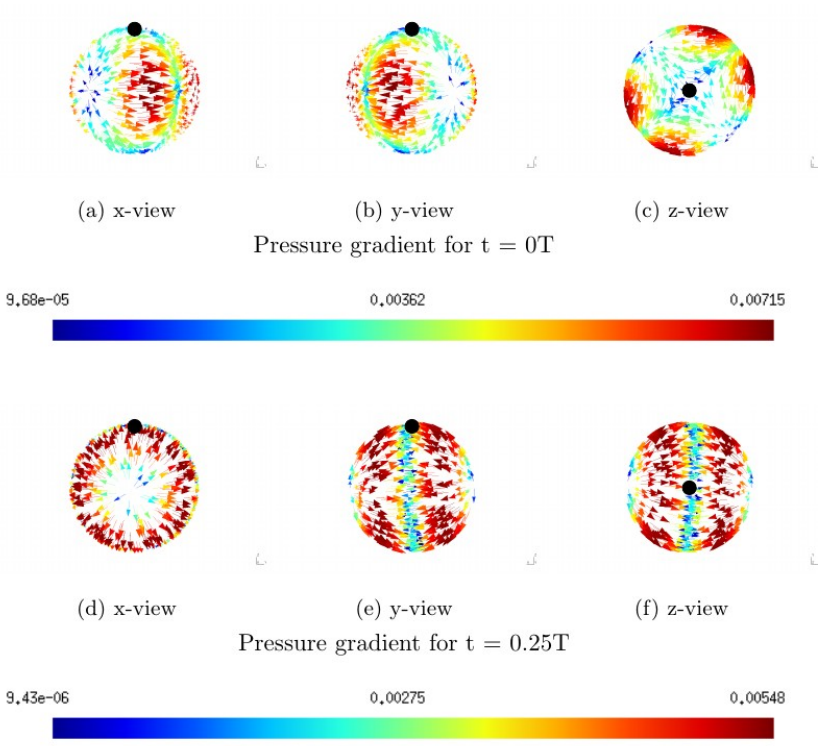


FIGURE 4.11: pressure gradient field for $h_2 = 1.1 + 0.75i$ [Pa]

Before doing that, I will look at the pressure gradient field for a Love number with a negative imaginary part. I choose the following one : $h_2 = 1.1 - 0.5i$. The picture can be seen on the figure 4.12. For t = 0T and for t = 0.25T, the field is perfectly

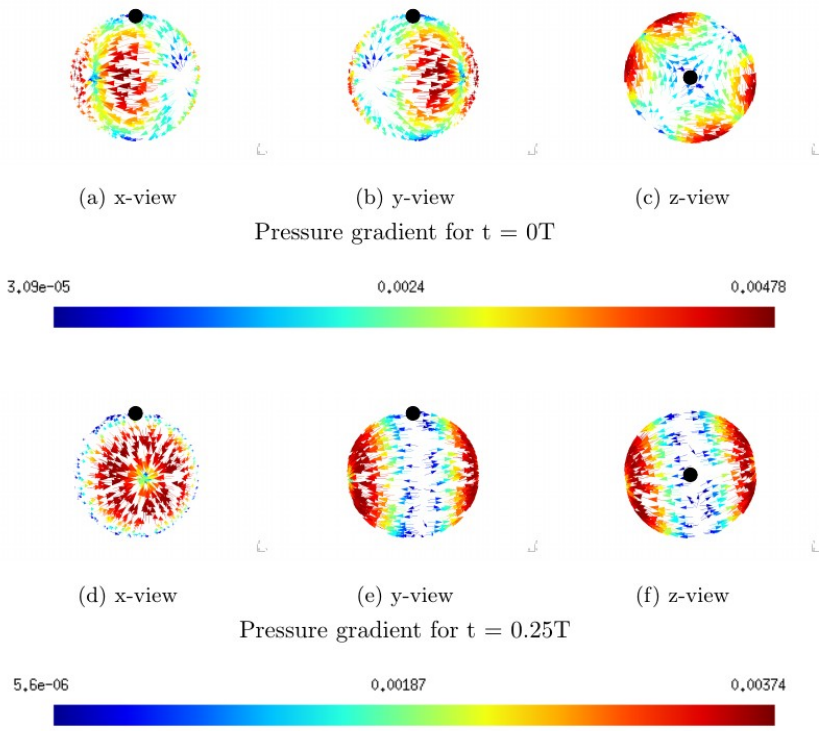


FIGURE 4.12: pressure gradient field for $h_2 = 1.1 - 0.5i$ [Pa]

symmetrical to the field for $h_2 = 1.1 + 0.5i$. This result confirms for good that the sign of the Love number has an effect on the sign of the phase shift.

Finally, to represent correctly the effect of the imaginary part of the Love number on the phase shift, I show the y-view for t = 0.25T and for many imaginary numbers. The results is showed on the figure 4.13. The question that can now be asked is :

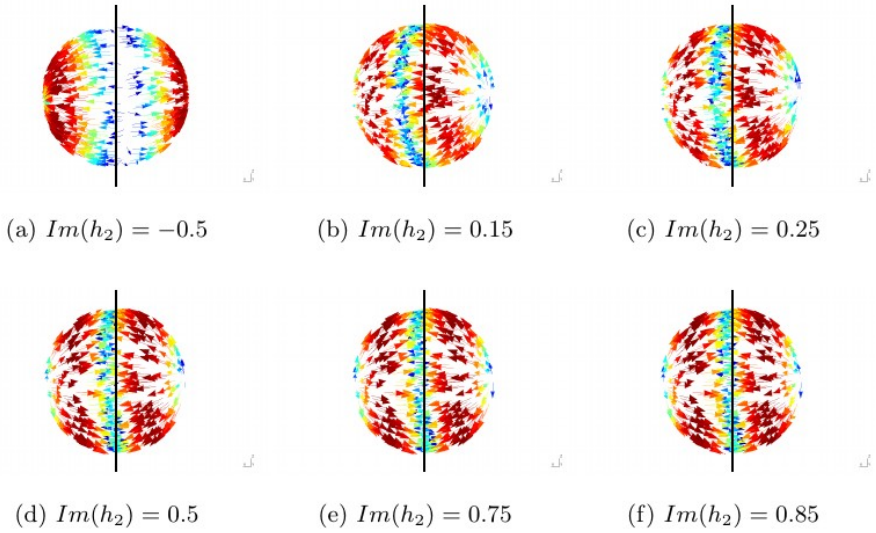


FIGURE 4.13: pressure gradient field for t = 0.25T and for the y-view [Pa]

"For which imaginary number the phase shift become $2\pi$?". If the proportion is kept,

as $0.5i$ correspond to $\phi = \frac{\pi}{4}$, I assume that $2i$ corresponds to $\phi = 2\pi$. I launched a simulation to check that. The results invalidate the assumptions. Consequently, the phase shift is not directly proportional to the imaginary part of the Love number. It would be interesting in another study or even another thesis to try to figure out the exact function describing the pressure gradient field in function the Love number. Maybe, this will lead to some better understanding of the tides of Titan, or more generally, of the tides of icy moons.

### 4.2.4 Summary

In this subsection I will summarize the three previous subsections. All the effects of the Love number on the pressure gradient field will be briefly described.

$R(h_2)$ The real part of the Love number only has an effect on the norm of the pressure gradient field. The bigger the real part is, the bigger the norm becomes. This is the only effect noticed.

$Im(h_2)$ The imaginary part of the Love number has two effects on the pressure gradient field. It adds a phase shift to this latter compared to the pressure gradient field of the pure real Love number. The function describing the phase shift in function of the imaginary part of $h_2$ seems to be an odd function. The bigger $|Im(h_2)|$ is, the bigger the phase shift becomes. Furthermore, $Im(h_2)$ also has influence on the norm. The function describing the evolution of the norm seems to behave like an absolute value function with a minimum at 0.

## 4.3 The Velocity field

In this section, I will analyze the influence of the Love number on the velocity fields. To see the results, I will just show the velocity fields and not the three components of the velocity. I will of course use the same Love number as before.

### 4.3.1 Pure real Love numbers

The first remark that can be made is that the norm of the velocity is quite small in comparison of the norm for the free elevation case. As a reminder, for $h = 10000m$, the maximum norm was $13.4\ 10^{-3}\ ms^{-1}$. The one for the real Love number are in the table 4.5.

| Love number | 1.1 | 1.2 | 1.3 | 1.4 |
|---|---|---|---|---|
| Maximum norm $[10^{-3}\ ms^{-1}]$ | 8.24 | 5.93 | 4.75 | 4.04 |

TABLE 4.5: Maximum norm of the velocity fields for real Love numbers

Contrary to the pressure gradient field, the norm of the velocity does not grow with the Love number. Thus, the true function describing the norm has to be a decreasing function. It is then interesting to know the minimum of this function. Indeed, the norm is by definition a nonnegative number but it is quite unlikely that the minimum is zero. Therefore, the most probable hypothesis is that the minimum goes on decreasing without never reach zero just like the inverse function. To confirm that hypothesis, I made an interpolation of the norm in function of the real part of $h_2$ on the figure 4.14. To obtain this interpolation, I had to launch a simulation for

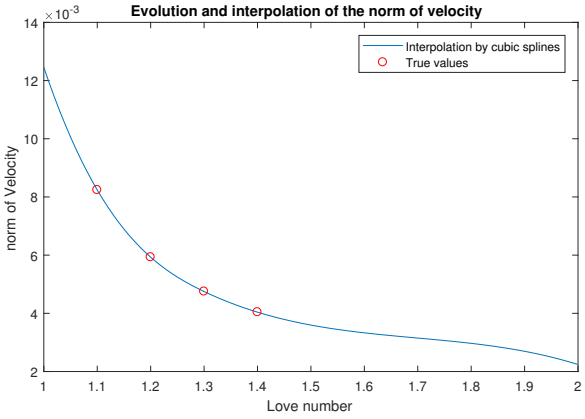


FIGURE 4.14: Interpolation of the norm of the velocity field for real Love numbers

$h_2 = 2$. The graph does confirm my hypothesis. The function just looks like the inverse function.

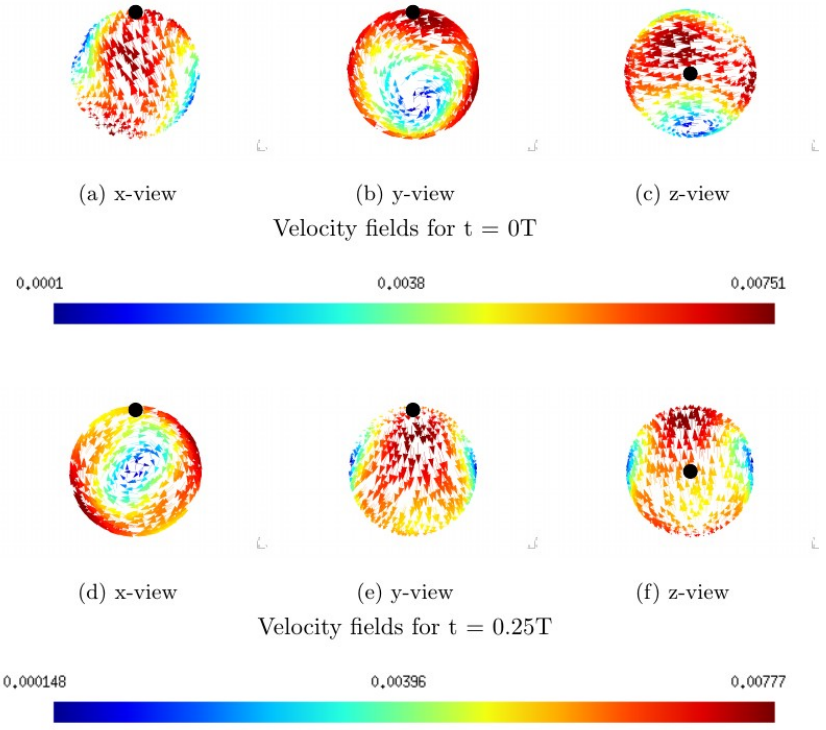


FIGURE 4.15: Velocity field for $h_2 = 1.1$ [$ms^{-1}$]

The velocity fields of the $h_2 = 1.1$ is represented on the figure 4.15. These are the only fields represented because the others Love numbers generated the same field. Furthermore, if you look carefully at the field for $h_2 = 1.1$, you will notice that the representation of the field is the same as the field obtained for the same depth in the previous chapter. Indeed, the maximum and the minimum values are located at the same regions. The directions of the arrows are also the same. This is true for the t = 0T and t = 0.25T. This result means that the real part of the Love number only has an effect on the norm of the velocity.

### 4.3.2 Complex Love numbers with the same imaginary part

| Love number | $1.1 + 0.5i$ | $1.2 + 0.5i$ | $1.3 + 0.5i$ | $1.4 + 0.5i$ |
|---|---|---|---|---|
| Maximum norm $[10^{-3}\ ms^{-1}]$ | 3 | 4.04 | 3.77 | 4.04 |

TABLE 4.6: Maximum norm of the velocity fields for complex Love numbers with the same imaginary part

Adding an imaginary part to the Love number decreases the norm of the velocity. The norms of the four complex $h_2$ simulated decrease compared to the pure real $h_2$. It even seems that the smaller the real part of the Love number is, the bigger the decrease compared to the pure real love number get. It can be seen by comparing the table 4.6 and the table 4.5. Indeed, the biggest maximum is the one of the Love number $1.2 + 0.5i$ while, for the real Love number, the bigger maximum norm of the velocity field was the one of the Love number 1.1. Moreover, I assume that the decrease of the norm has a limit. By that, I mean that I assume the norm never becomes zero for any imaginary part. This will be analyzed in the next subsection.

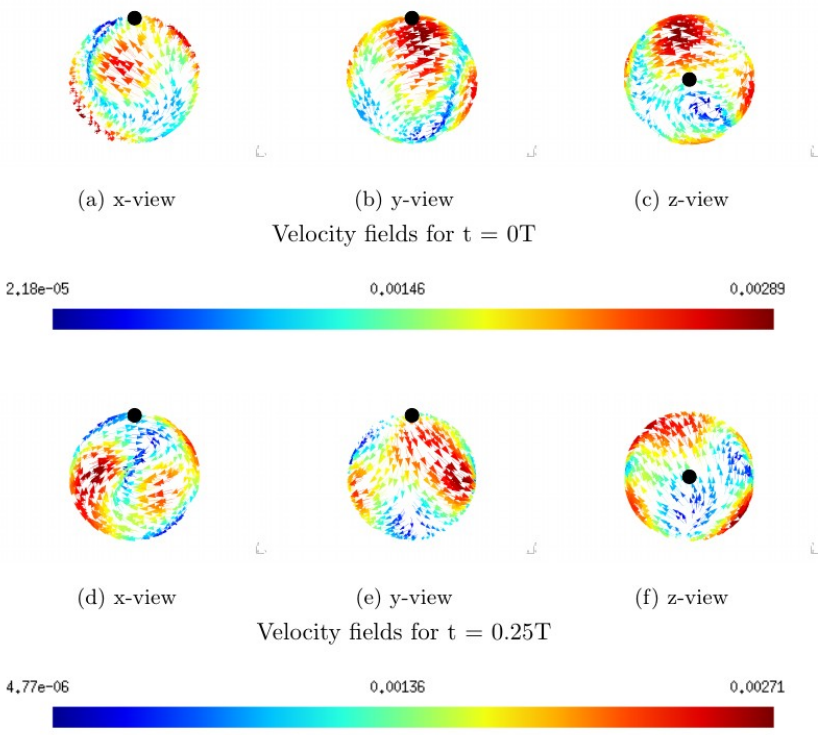


FIGURE 4.16: Velocity field for $h_2 = 1.1 + 0.5i$ $[ms^{-1}]$

The velocity field can seen on the figure 4.16. This time, the velocity field is not the same as in the previous chapter. The figure does not even look like any figure shown before. Furthermore, the representation of the field is too complicated to be described precisely. I will then just describe the simplest characteristic. The maximum values of the velocity field are located in three regions. These regions are more or less circular. The region of the minimum values is quite complex. The arrows of the velocity field are oriented to two circular areas. The areas are located at two opposite points in the

GSO. Eventually, it is interesting to notice that this velocity field look exactly like the one of a depth of 1000m for the free elevation case (see figure 3.19 ).

### 4.3.3 Complex Love numbers with same real part

| Love number | $11 - 0.5i$ | $11 + 0.15i$ | $11 + 0.25i$ | $11 + 0.5i$ | $11 + 0.75i$ | $11 + 0.85i$ |
|---|---|---|---|---|---|---|
| Norm max [$10^{-3}$ m$s^{-1}$] | 4.61 | 6.53 | 5.41 | 3 | 4.09 | 4.09 |

TABLE 4.7: Maximum norm of the velocity field for complex Love numbers with the same real part

In the table 4.7, the norms of the velocity are shown. The results are quite impressive. They show that the norm reaches a maximum at $h_2 = 1.1 + 0i$ (norm = 8.24 $10^{-3}$). Then, adding a positive or a negative imaginary part to the Love number only decreases the norm. This decrease does not seems to last for ever. From a certain value of $Im(h_2)$, the norm seems to increase again after passing by a minimum. To check that assumption, I looked at the results for $h_2 = 1.1 + 1i$ and for $h_2 = 1.1 + 2i$. The maximum norms for these Love numbers are respectively 4.13 $10^{-3}$m$s^{-1}$ and 4.61 $10^{-3}$m$s^{-1}$. Thus, it seems that the function describing the norm in function of $Im(h_2)$ has many extrema. To represent that function, I made an interpolation on figure 4.17. Unfortunately, this interpolation function does not look like anything simple known function.

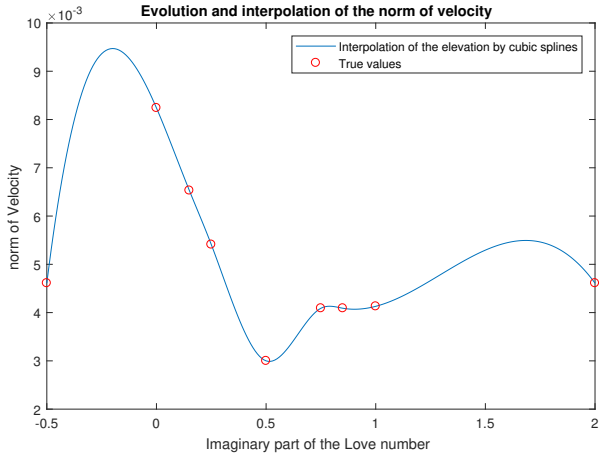


FIGURE 4.17: Interpolation of the norm of the velocity field for complex Love numbers with the same real part

Eventually, the velocity fields of the Love number with the same real part are all the same. Consequently, the conclusion is that changing $Im(h_2)$ only does have effect on the norm. It is the same conclusion I reached when I analyzed the influence of the real part of the Love number.

### 4.3.4 Summary

The conclusion of the study of the influence of $h_2$ on the velocity field are pretty different from the study of the influence on the pressure gradient field. The Love number mainly has effect on the norm of the velocity. They can no longer generate

any phase shift. Adding imaginary part to the Love number changes the velocity fields. However, changing its value has no effect on the fields. Moreover, increasing the real part only decreases the norm while increasing the imaginary part can decrease or increase the norm.

## 4.4 The others depths

In the previous section, I have had results for a depth of 10000m. From these results, I made conclusions about the effect of the Love number on the pressure gradient field and the velocity field. However, I focused only on one depth. Consequently, if I want to be the most critic possible, I have to check the conclusions obtained for at least one other depth. I have decided to test the effect of the Love number for a depth of 5000m. I chose this depth because, when I studied the free elevation case, this latter generated the most interesting results. Furthermore, its principal tidal components have the highest orders.

### 4.4.1 The pressure field

After launching the simulations for a few real and complex Love numbers, I obtain the same the pressure fields as those one obtained for $h = 10000m$. The fields have the same representations. The only differences are the maximum and minimum norms of the pressure gradient field. As proof, on figure 4.18, one can see the field for $h_2 = 1.1$ and for t = 0T. Furthermore, the norms follow the same pattern as the

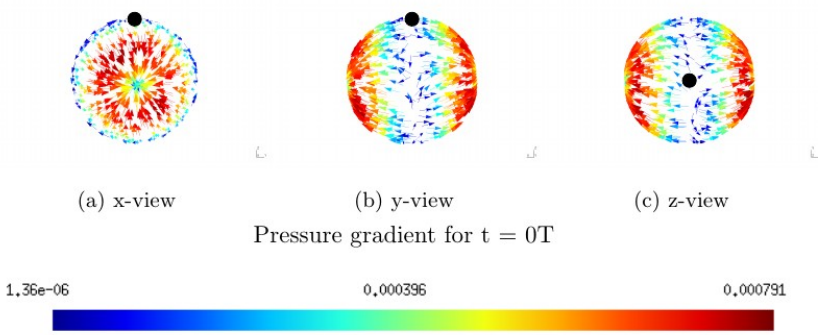


FIGURE 4.18: Pressure gradient field of $h_2 = 1.1$ for $h = 5000m$ [ms$^{-1}$]

ones for $h = 10000m$. The bigger the real part and the absolute value of the imaginary part of the Love numbers are, the bigger the norms are. Eventually, the phase shifts, which appear for complex Love numbers, seem to behave like the the ones discussed for a depth of 10000m

### 4.4.2 The velocity field

Once more, the results are similar to the one obtained before. The velocity fields have the same representations and behaviors. On figure 4.19, the fields for $h_2 = 1.1$ and for t = 0T can be seen. Only the extrema of the norms change. The real and complex Love numbers have the same influence on the latter as the one described before. Furthermore, the velocity fields never does suffer from a phase shift whatever the Love numbers.

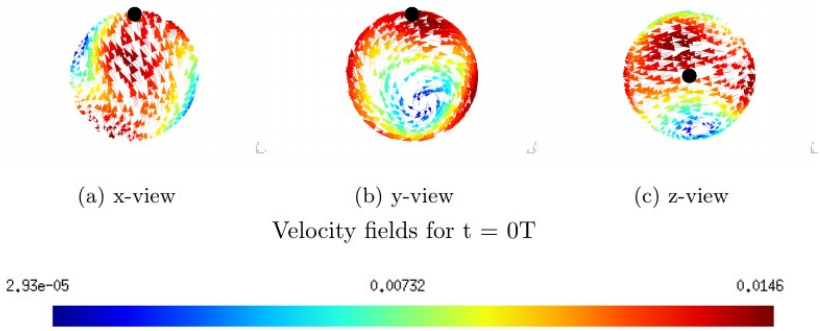


FIGURE 4.19: Velocity field of $h_2 = 1.1$ for $h = 5000m$ [ms$^{-1}$]

# Chapter 5

# Conclusion

In this master's thesis, I presented Titan and its specificity. One of its most interesting feature is the existence of a global subsurface ocean. This ocean located under the icy crust was the main interest. More precisely, all the interest was focused on the tides and their characteristics. In chapter 2, I globally described Titan and its structure. Then, I presented and developed the shallow-water equations, the equations governing the motion of the tides. I applied and modified this equations for my specific case. This gave the modified SWE :

$$\begin{cases} \frac{\partial \mathbf{u}}{\partial t} + \mathbf{u} \cdot \boldsymbol{\nabla} \mathbf{u} + f \mathbf{e}_z \wedge \mathbf{u} + g \boldsymbol{\nabla} \eta + \frac{1}{\rho} \boldsymbol{\nabla} p_s = \frac{1}{H} \boldsymbol{\nabla} \cdot (H \nu \boldsymbol{\nabla} \mathbf{u}) + \frac{\boldsymbol{\tau}^s - \boldsymbol{\tau}^b}{\rho H} + \boldsymbol{\nabla} U \\ \frac{\partial \eta}{\partial t} + \boldsymbol{\nabla} \cdot (H \mathbf{u}) = 0 \end{cases}$$

The elevation being now a known variable, I proposed two models. The first one considers that the crust is perfectly elastic. Therefore, the ocean acts like there is no surface above it. The second model considers that the tides are generated by a tidal potential.

Afterwards, in chapter 3, I analyzed the results obtained with SLIM for the first model for several different depths. The elevation of each depth was close to 10m. The main tidal component was always the first one. However, for some depth, the elevation suffered the effect of others tidal components. For instance, for $h = 5000$m, the representation of its elevation showed that the tidal bulges change a lot in a few instants. Furthermore, for low depths like $h = 100$m, a little phase shift appeared. I supposed that this phase shift occurred because these depths were really small in comparison to the thickness of the surface above and behind.

I also looked at the velocity field of each depth. The maximum norm decreased with the depth. Moreover, the representation of the velocity field changed a lot from a depth to another. With all these results, I concluded that the ocean depth has a significant impact on the tidal flow.

Afterwards, in chapter 4, I looked at the results obtained for the second model. For the Love number, I looked at articles proposing different ranges for the real part and the imaginary part. Then, I analyzed the results for several different Love numbers and for $h = 10000$.

Concerning the pressure gradient field, for each real $h_2$, its representation was the same. In fact, the real part of the Love number only had effect on the norm of the pressure gradient fields. This latter grew linearly with the real part of $h_2$. Adding imaginary part to $h_2$ has two effects. The first effect was to add a phase shift. The function describing this phase shift in function of the imaginary part of the Love number seemed to be a odd function. The second effect was to increase the norm

of the pressure gradient field. The function describing the increase followed the behavior of an absolute value function.

Concerning the velocity field, again its representation did not change whatever the real $h_2$. This time, the real part of the love number decreased the norm of the field. The decrease seemed to be inversely proportional to this latter. Adding imaginary part to $h_2$ has two effects. It decreased the norm of the velocity fields and it changed completely its representation.

Finally, to confirm the results, I looked at some results for a different depth. For all the real and the complex Love numbers, I obtained the same pressure gradient fields and velocity fields. Therefore, for this model, I concluded that the mechanical properties of the ice shell significantly modify the tidal flow while the depth of the ocean does not influence it.

To conclude, let I mention the prospects of amelioration that come to my mind. Firstly, I suggest finding the functions describing the impact of the complex Love number on the pressure gradient field and the velocity field. If these functions are too complex to be obtained, then approximations could also be interesting. Secondly, I propose to extend SLIM for the simulation of the tidal dissipations. Doing so, one could obtain a representation of the heat produced by these dissipations. It could be interesting given that this latter helps maintaining the ocean liquid. Finally, I think it would be interesting to test all the code and all the simulation for one or more others icy moons. This way, one can see if the results of this master's thesis are specific to Titan or if they represent the general behavior of every icy moon.

# Appendix A

# Bibliography

[Beu15a] M. Beuthe. Tidal Love number of membrane worlds: Europa, Titan, and co. *Icarus.*, 248(1):239–266, 2015.

[Beu15b] M. Beuthe. Tides on Europa: The membrane paradigm. *Icarus.*, 248(1):109–134, 2015.

[Eri18] K. Erickson. Titan, May 2018.

[FG09] M.A. Fernández and JF. Gerbeau. Algorithms for fluid-structure interaction problems. In *Cardiovascular Mathematics*, chapter 9, pages 307–346. Springer, Milano, 2009.

[For11] A.D. Fortes. Titan's internal structure and the evolutionary consequences. *Icarus..*, 60(1):10–17, 2011.

[FSL03] T. Spohn F. Sohl, H. Hussmann and R.D. Lorenz. Interior structure models and tidal Love numbers of Titan. *Journal of geophysical research*, 108(E12), 2003.

[GL12] J.C. Goodman and E. Lenferink. Numerical simulations of marine hydrothermal plumes for Europa and other icy worlds. *Icarus.*, 221(2):970–983, 2012.

[GTS05] A. Mocquet G. Tobie and C. Sotin. Tidal dissipation within large icy satellites: Applications to Europa and Titan. *Icarus.*, 177(2):534–549, 2005.

[OF10] C.Sotin O.Grasset and F.Deschamps. On the internal structure and dynamics of Titan. *Icarus..*, 48(7-8):617–636, 2010.

[Rus04] R. Russell. Windows to the universe, June 2004.

Rue Archimède, 1 bte L6.11.01, 1348 Louvain-la-Neuve **www.uclouvain.be/epl**